1 **Supporting information for "Volatility and lifetime against OH heterogeneous reaction of**
2 **ambient Isoprene Epoxydiols-Derived Secondary Organic Aerosol (IEPOX-SOA)"**

3 Weiwei Hu[1,2], Brett B. Palm[1,2], Douglas A. Day[1,2], Pedro Campuzano-Jost[1,2], Jordan E.
4 Krechmer[1,2], Zhe Peng[1,2], Suzane S. de Sá[3], Scot T. Martin[3,4], M. Lizabeth Alexander[5], Karsten
5 Baumann[6], Lina Hacker[7], Astrid Kiendler-Scharr[7], Abigail R. Koss[1,2,8], Joost A. de Gouw[1,2,8],
6 Allen H. Goldstein[9,10], Roger Seco[11], Steven J. Sjostedt[8], Jeong-Hoo Park[12], Alex B. Guenther[11],
7 Saewung Kim[11], Francesco Canonaco[13], André. S. H. Prévôt[13], William H. Brune[14], Jose L.
8 Jimenez[1,2]

9 1 Cooperative Institute for Research in Environmental Sciences, University of Colorado,
10 Boulder, CO, USA 80309
11 2 Department of Chemistry and Biochemistry, University of Colorado, Boulder, CO, USA 80309
12 3 John A. Paulson School of Engineering and Applied Sciences Harvard University, Cambridge,
13 MA, USA 01742
14 4 Department of Earth and Planetary Sciences, Harvard University, Cambridge, MA, USA 01742
15 5 Environmental Molecular Sciences Laboratory, Pacific Northwest National Laboratory,
16 Richland, WA, USA 99352
17 6 Atmospheric Research and Analysis Inc., Morrisville, NC, USA 27560
18 7 Institute for Energy and Climate Research - Troposphere (IEK-8), Forschungszentrum Jülich,
19 D-52425 Jülich, German
20 8 Earth System Research Laboratory, NOAA, Boulder, Colorado, USA 80305
21 9 Department of Environmental Science, Policy, and Management, University of California,
22 Berkeley, CA, USA 94720
23 10 Department of Civil and Environmental Engineering, University of California, Berkeley, CA,
24 USA 94720
25 11 Department of Earth System Science, University of California, Irvine, USA 92697
26 12 National Institute of Environmental Research, Republic of Korea 22689
27 13 Laboratory of Atmospheric Chemistry, Paul Scherrer Institute (PSI), 5232 Villigen,
28 Switzerland
29 14 Department of Meteorology, Pennsylvania State University, University Park, PA, USA 16802
30 Correspondence to: J. L. Jimenez (jose.jimenez@colorado.edu)

31

32

1. AMS setup and operation

Non-refractory submicron particle-phase mass concentrations at both field sites were measured by an Aerodyne High Resolution Time-of-Flight Aerosol Mass Spectrometer (HR-ToF-AMS, hereafter called AMS) to quantify OA, sulfate, nitrate, ammonium, and chloride (DeCarlo et al., 2006) and oxygen-to-carbon (O/C) and hydrogen-to-carbon (H/C)ratios of OA (Aiken et al., 2008; Canagaratna et al., 2015). An aerodynamic lens (Zhang et al., 2004) focuses submicron particles into a narrow beam, followed by evaporation after impacting a 600 $^{\circ}$C porous tungsten inverted-cone vaporizer, and analysis of the vapors by electron impact (EI) and time-of-flight mass spectrometry. Data analysis was performed using standard AMS software (SQUIRREL1.52M, PIKA1.15D) available online (webpage: http://cires1.colorado.edu/jimenez-group/ToFAMSResources/ToFSoftware/index.html).

For SE US (SOAS) study, the AMS sensitivity and ammonium relative ionization efficiency (RIE) were calibrated every few days (~3 days typically) using dried 400 nm (mobility diameter) ammonium nitrate particles. The variation of the ratio of ionization efficiency to the airbeam signal (IE/AB), a proxy for stability of instrument sensitivity, was within 5% across the whole campaign. The sulfate RIE (~1.3) was calibrated multiple times during the campaign, the variation of which was within 3%. Time-dependent collection efficiency (CE) was estimated using the composition-dependent formulation of Middlebrook et al. (2012), and usually varied between 0.5-0.7 in both ambient and OFR conditions. Good agreement of volume concentration between AMS and SMPS were observed, supporting the quantification of the AMS during this study (Fig. S5). Ambient air was sampled at 10 liters per minute (LPM) via a PM2.5 cyclone (URG corporation) at ambient temperature and humidity, immediately followed by a multi-tube nafion drier (Perma Pure LCC, PD-50T-12-MSS), then through a 0.375" OD and 0.311" ID 2.5 m long stainless steel tube into the temperature-controlled trailer. RH in the 10 LPM flow once in the trailer was always <60% (typically <50%). Within the trailer, 0.7 LPM was split from the main flow for sampling by the AMS and SMPS (tube of 0.25" OD, 0.194" ID after split), passed through a single-membrane nafion drier (Perma Pure LCC, MD-110-24S-4) to reach RH <30%, and 0.1 LPM was sampled by the AMS and 0.3 LPM by the SMPS. The flow was laminar throughout the entire inlet, and the total residence time was approximately 6 s.

2. Quantification of IEPOX-SOA in the oxidation flow reactor (OFR) and TD datasets

The IEPOX-SOA factors for the OFR and TD dataset were obtained using the constrained positive matrix factorization (PMF) method, as implemented in the multilinear engine (ME-2) software. The full ambient IEPOX-SOA spectrum (high resolution; m/z 12-120; 302 fitted high-resolution ions) obtained from unconstrained PMF of the ambient data was used as a constraint. The theoretical principles and application of PMF and ME-2 are described by Paatero et al. (1997; 1999), Ulbrich et al. (2009), and Canonaco et al. (2013). ME-2 was run via the SoFi interface v. 5.3 (Canonaco et al., 2013). For the ME-2 setup, a range of a-values between 0-0.2 and 0.5 (fully constrained to partially constrained) were tested in the OFR and TD datasets, respectively. We found consistent retrieval of IEPOX-SOA for different a-values in both OFR (slope range: 0.93-1.14; R>0.99) and TD datasets (slope range: 0.96-1.07; R>0.99), as shown in Fig. S6 and S8, which supports the robustness of IEPOX-SOA retrieval in this study. Consistency of mass fraction remaining for IEPOX-SOA at different a values as a function of OH exposure and TD temperature, respectively, were also observed for different a-values within ME-2 (Fig. S7 and Fig. S9). IEPOX-SOA factors with a-value=0 from both datasets (i.e. fully constrained spectrum) were used in this study.

Besides constraining the ambient IEPOX-SOA spectrum in ME-2 fot the TD dataset to obtain a IEPOX-SOA thermogram, we also ran unconstrained PMF ("free PMF", using PET and PMF2. exe) on the OA matrix for the combined ambient and TD datasets. The heating process in TD unlikely will make new OA sources (Huffman et al., 2009), and thus this method allows deriving an alternative IEPOX-SOA thermogram. Finally, thermograms of IEPOX-SOA derived with both methods show similar variations (Fig. S9), which provides additional confidence in the data used to evaluate the volatility of IEPOX-SOA in Section 3.2 of the main text.

3. Box model setup

3.1 Model setup

To investigate the fate of gas-phase IEPOX in the OFR, a box model was run with the mechanism shown in Table S2 and Fig. 3. This box model assumes that no NO is present, since NO in SE US study was only ~60 ppt on average in the daytime atmosphere and its lifetime in the OFR is very short (~1 s, Li et al., 2015; Peng et al., 2015). This model ignored the slightly different reaction rates among isomers of IEPOX and isoprene hydroxyhydroperoxide (ISOPOOH)with OH radical (Bates et al., 2015; Krechmer et al., 2015), thus it is a simiplied

93   version. The average measured diurnal variations of isoprene, ISOPOOH and IEPOX

94   concentrations were used as input concentrations, as shown in Fig. S1. Isoprene, ISOPOOH and

95   IEPOX show consistently high concentrations in the afternoon, as expected based on the current

96   understanding of their temperature and light-dependent emissions (isoprene) and photochemical

97   formation mechanisms (ISOPOOH and IEPOX) (Paulot et al., 2009). We chose the peak

98   concentrations of the three species during the day as initial input into the model, which are 5.8

99   ppb for isoprene, 181 ppt for ISOPOOH and 70 ppt for IEPOX, respectively. The main reaction

100   parameters in the model are described in Table S2.

101   In the model, the dynamic OH exposures in ambient and OFR cases were achieved

102   according to the real ambient and OFR conditions. In the ambient scenario, different OH

103   exposures were calculated by only varying the reaction time (0-60 days). A fixed OH

104   concentration of 1.5×10^6 molec. cm^{-3} was set (Mao et al., 2009). In the OFR scenario, reaction

105   time was fixed (at the residence time of 200s), and a range of OH exposures was obtained by

106   varying the OH concentrations in the model, which were controlled in practice by the RH and the

107   UV light settings in the OFR.

108   *3.2 Organic/inorganic scenarios vs inorganic scenarios in the model*

109   A model scenario accounting for organic resistance with slower IEPOX uptake than pure

110   inorganic is applied to simulate the fate of gas-phase IEPOX. In the inorganic-only aerosol

111   uptake scenario, γ_{IEPOX} was calculated from the model assuming no organic resistance for gas-

112   phase IEPOX uptake. Gaston et al. (2014) showed that a lower γ_{IEPOX} was observed for mixed

113   polyethylene glycol (PEG)/ammonium bisulfate aerosols compared to pure ammonium bisulfate

114   aerosols, and attributed it to rate-limiting gas-phase IEPOX diffusion in the OA layer. In SE US,

115   OA composed 67% of ambient PM$_1$ mass on average and the fraction of OA was typically even

116   higher in the OFR due to greater addition of OA mass than inorganics (Fig. S15). You et al.

117   (2013) suggested an organic and inorganic phase separation can happen in particles with mixed

118   OA and inorganics (e.g. $(NH_4)_2SO_4$) at O/C<0.8. O/C ratios in OA were always lower than 0.8

119   for ambient conditions, while after the OFR they were below 0.8 at lower OH exposures

120   ($<3\times10^{11}$ molecular cm^{-3} s, ~3 equivalent days) and above at high exposures (not shown). The

121   newly formed oxidized gas-phase organic compounds may also condense on the surface of

122   aerosols to form fresh organic-dominated layers. If either effect (phase separation or organic

123   condensation) does occur, the OA "layer" will lead to a smaller effective γ_{IEPOX} than the values

124   calculated by assuming aerosols are composed of pure inorganic species in the model (Gaston et

125   al., 2014). Thus, eventually, accounting for organic resistance to IEPOX aerosol uptake is more

126   realistic for ambient IEPOX uptake modeling results, which will be discussed in the main text.

127   The results from inorganic scenario can be found in Fig. S16.

3.3 pH and aerosol uptake coefficient of IEPOX

129   Estimated γ_{IEPOX} is crucial to determine the lifetime of IEPOX against aerosol uptake.

130   γ_{IEPOX} is affected by several factors, e.g. the mass accommodation coefficient α_{IEPOX},

131   acidity/sulfate (nucleophilic effect), aerosol size, and organic resistance on the particle (Gaston et

132   al., 2014; Nguyen et al., 2014a; Xu et al., 2014; Liao et al., 2015). γ_{IEPOX} can be estimated based

133   on a modified resistor model described in Gaston et al. (2014). The predicted γ_{IEPOX} from this

134   model has been shown to be in good agreement with measured γ_{IEPOX} in laboratory studies

135   (Gaston et al., 2014). To estimate γ_{IEPOX} for ambient and OFR condition during SE US study,

136   the estimated aerosol pH for both conditions is needed.

137   The pH values of aerosols under ambient and OFR conditions were calculated by with both

138   the E-AIM II (Wexler and Clegg, 2002) (Web: http://www.aim.env.uea.ac.uk/aim/aim.php) and

139   ISORROPIA II (Fountoukis and Nenes, 2007) (Web:

140   http://isorropia.eas.gatech.edu/index.php?title=Main_Page) thermodynamic models (Fig. S10-

141   S11). Good agreement for the estimated pH between the two models was found in both

142   conditions. Since extra parameters from E-AIM II output (e.g. concentration of nucleophile) are

143   needed to calculate the γ_{IEPOX} in the model, the pH calculated from E-AIM II was used as the

144   input in our model. Average pH values from E-AIM II in ambient and OFR aerosol during SE

145   US study were 0.8±0.5 and 1.35±0.6, respectively. The pH values of 1.33-1.51 over OH

146   exposure in the OFR was found in Fig. S12a, contrast to a clear enhanced predicted

147   NH_4/measured NH_4 ratio (0.55-0.75) in Fig. S12b. The predicted NH_4 concentration was

148   calculated based on assuming fully neutralization of aerosol between anion and cation ions. The

149   seemingly inconsistent trend between calculated pH and NH_4 balance as a function of OH

150   exposure is consistent with the conclusion that NH_4 imbalance does not have a unique

151   relationship with pH under very acidic conditions (Hennigan et al., 2015). Finally, pH values of

152   0.8 and 1.35 were input into the model for ambient and OFR scenarios, respectively.

153   The other main parameters input into the model include temperature (298K), mass

154   accommodation coefficient (0.1) (Gaston et al., 2014), particle radius (140 nm, Fig. S12c),

155   concentration of nucleophiles including SO_4^{2-} and NO_3^- (~ 0.05±0.1 M and 0.23±0.23 M in

156   ambient and OFR respectively) and HSO_4^- concentration (0.59±2.4 M and 0.09±0.12 M)

157   obtained from the output of E-AIM II model. In the calculation, aerosols with and without an

158   organic film resistance were assumed. In the case that assumes aerosol is composed of pure

159   inorganic species, the calculated γ_{IEPOX} was 0.025 and 0.008 under ambient and OFR conditions,

160   respectively. In the more realistic case that assumes an organic resistance to mass transfer, the

161   calculated γ_{IEPOX} were 0.009 and 0.002 under ambient and OFR conditions, respectively. In the

162   organic resistance case, the radius of the inorganic core was input in the model, which was

163   estimated to be 100 nm from the organic/inorganic volume ratio estimated from the AMS data.

164   A factor of 0.1 was applied to decrease the Henry's law constant and diffusivity of IEPOX in the

165   organic film (Gaston et al., 2014).

166   In SE US study, the total aerosol surface area of ambient submicron aerosol was around

167   300±230 μm^2 cm^{-3} based on SMPS measurements, while a higher average surface area of

168   submicron aerosol (350±550 μm^2 cm^{-3}) was observed in OFR, as shown in Fig S23-S24.

169   Internally mixing of organic and inorganic was assumed here based on single particle mass

170   spectrometer results (Lee et al., 2002). The higher aerosol surface areas in OFR was mainly

171   caused by the condensation of newly formed low-volatility VOCs species and a small fraction of

172   newly-formed inorganic species. Finally, the calculated reaction coefficients of IEPOX uptake

173   onto aerosol are 4.3×10^{-4} s^{-1} (lifetime=0.6 h) and 1.6×10^{-4} s^{-1} (lifetime=1.7 h) under ambient and

174   OFR conditions (respectively) with pure inorganic species, and 1.5×10^{-4} s^{-1} (lifetime=1.8 h) and

175   4.0×10^{-5} s^{-1} (lifetime=7.0 h) under ambient and OFR conditions (respectively) under the

176   assumption of organic resistance to mass transfer.

177   *3.4 Photolysis of isoprene, ISOPOOH and IEPOX*

178   The photon fluxes inside the OFR were calculated by a dynamic chemistry model based on

179   SE US scenario (Peng et al., 2015). The main emission lines of the UV light spectrum of the

180   mercury lamp are at 185 nm and 254 nm. The photon fluxes at 185 nm and 254 nm in SE US

181   range between 5×10^9-3×10^{13} photon cm^{-2} s^{-1} and 1×10^{12}-3×10^{15} photon cm^{-2} s^{-1}, respectively,

182   with ambient RH 80% assumed. The roles of photolysis in the decays of the main gas species

183   (i.e., isoprene, ISOPOOH and IEPOX) in the model were investigated.

184   The absorption cross sections of isoprene at 185 and 254 nm are around 1.35×10^{-17} cm^2

185   molec.$^{-1}$ and very small that we assumed 0 cm^2 molec.$^{-1}$ at 254 nm, respectively (Martins et al.,

186   2009). No IEPOX and ISOPOOH cross section nor quantum yield data have been reported in this

187   UV spectral region. Here, we used measured cross section data of 3-hexene-1-ol ($C_6H_{12}O$)

188   (2×10^{-17} cm^2 molec.$^{-1}$ at 185 nm and 1×10^{-21} cm^2 molec.$^{-1}$ at 254 nm) to simulate IEPOX

189   ($C_5H_{10}O_3$) due to their similar carbon backbone and functional groups (hydroxyl group) (Jiménez

190   et al., 2009), and 2-hexanone-5-hydroperoxide ($C_6H_{12}O_3$) for ISOPOOH (1.1×10^{-17} cm^2 molec.$^{-1}$

191   at 185 nm and 6×10^{-19} cm^2 molec.$^{-1}$ at 254 nm) (Jorand et al., 2000). The chromophore in IEPOX

192   at 185 nm is epoxide. Some epoxides themselves do absorb at 185 nm however, the detected

193   cross section is a few times lower than 2×10^{-17} cm^2 molec.$^{-1}$ (Fleming et al., 1959). Thus values

194   from 3-hexene-1-ol should result in upper limits of photolysis rates for IEPOX, since the

195   conjugated structure in 3-hexene-1-ol will result in higher light absorption than IEPOX in the

196   UV light range. The chromophore in ISOPOOH at 185 nm is double bond and hydroperoxide. The

197   detected cross section of both functional group at 185 nm are also below 10^{-18} cm^2 molec.$^{-1}$(Keller-

198   Rudek et al., 2013), which is smaller than the value (1.1×10^{-17} cm^2 molec.$^{-1}$) applied in the model.

199   The summary of cross sections of these three species is shown in Table S3. With quantum yields

200   of 1 assumed, the calculated photolysis fractions of these three gas species all less than 0.4 %,

201   representing a very minor fate across the entire OH exposure range in the OFR.

202   *3.5 Dry deposition of IEPOX*

203   The dry deposition velocity of IEPOX during SE US study was measured by Nguyen et al.

204   (2015), and reported as 3 cm s^{-1} in the afternoon. The measured boundary layer height in the

205   afternoon during SE US study is around 1200 m (Su et al., 2015). Thus the calculated dry

206   deposition loss rate of IEPOX is 2.5×10^{-5} s^{-1}, equivalent to an 11-hour lifetime.

207

208

209   **Table S1** Instruments for measurement of gas and aerosol phase species in this study.

Instruments name	Abbreviation name	Species measured	Time resolution	Manufacturer	References
Aerosol-phase					
High-resolution time-of-flight aerosol mass spectrometer.	HR-ToF-AMS	$NR-PM_1$ and its main species	2 min for V mode; 2 min for W mode	Aerodyne Research Inc., USA	(DeCarlo et al., 2006)
Scanning mobility particle sizer (DMA model 3805; CPC 3760)	SMPS	Number size distribution (13-600 nm)	4 min	TSI Inc., USA	(Stolzenburg et al., 1998)
Gas-phase					
Proton-transfer-reaction time-of-flight mass spectrometry	PTR-TOF-MS	Gas phase volatile organic compounds	10 s	Ionicon Analytik, Austria	(Jordan et al., 2009)
Picarro G2301 analyzer	Picarro CO analyzer	CO, CO_2, CH_4, H_2O	10 s	Picarro, Inc., USA	(Chen et al., 2013)
O_3 analyzer Model 205 Monitor	O_3 analyzer	O_3	1 min	2B Technologies	(Johnson et al., 2014)
Vaisala HM70 probe.	Vaisala HM70 probe.	Ambient RH, temperature, water vapor.	10 secs	Vaisala inc.	(CreĠu, 2008)

210

211

212

213 **Table S2** Initial input parameters and reactions for the IEPOX fate model.

Species or condition	Initial value
OH	7.5×10^6-2.4×10^{10} molec. cm^{-3} for OFR scenario
	1.5×10^6 molec. cm^{-3} for ambient scenario
Isoprene	5.8 ppb
IEPOX	70 ppt
ISOPOOH	181 ppt
Temperature	25 °C
RH	80%
Pressure	1013 mbar

Reaction	Rate Coefficient at 25 °C (cm^3 molec.$^{-1}$ s^{-1} unless noted otherwise)	Reference
Isoprene+OH $\rightarrow$ ISOPOOH	7×10^{-11}	(Atkinson and Arey, 2003)
ISOPOOH + OH $\rightarrow$ IEPOX	5.27×10^{-11}	(Paulot et al., 2009; Xie et al., 2013)
ISOPOOH + OH $\rightarrow$ LVOC$_{ISOPOOH}$	1.77×10^{-11}	(Krechmer et al., 2015)
IEPOX + OH $\rightarrow$ Other Products	1.0×10^{-11}	(Bates et al., 2014)
LVOC$_{ISOPOOH}$ $\rightarrow$ ISOPOOH-SOA	6.6×10^{-3} s^{-1}	(Krechmer et al., 2015)
IEPOX $\rightarrow$ IEPOX-SOA	4.0×10^{-5}–4.3×10^{-4} s^{-1}	(Gaston et al., 2014)
IEPOX+hv $\rightarrow$ IEPOX photolysis products	1×10^{-7}–6×10^{-4} s^{-1}	(Jiménez et al., 2009)

214

215

216 **Table S3** Cross sections and photolysis fractions of several key model species at 185 and 254 nm

217 in the OFR. The photon fluxes of 185 and 254 nm in OFR were calculated as part of the box model

218 described in Peng et al. (2015), which ranged between 5×10^9-3×10^{13} photon cm^{-2} s^{-1} and 1×10^{12}-

219 3×10^{15} photon cm^{-2} s^{-1}, respectively. Quantum yield=1 was used here to obtain upper limits for the

220 photolysis fractions.

Species	Cross section at 185 nm (cm^2 $molec.^{-1}$)	Cross section at 254 nm (cm^2 $molec.^{-1}$)	Sum photolysis fraction (%)	References
Isoprene	1.35×10^{-17}	0	<0.2	(Martins et al., 2009)
IEPOX	2×10^{-17}	1×10^{-21}	<0.4	(Jiménez et al., 2009)
ISOPOOH	1.1×10^{-17}	6.0×10^{-19}	<0.01	(Jorand et al., 2000)
IEPOX-SOA	2.5×10^{-17}	2.50×10^{-19}	<1.5	(Lin et al., 2014)

221

222

223

224
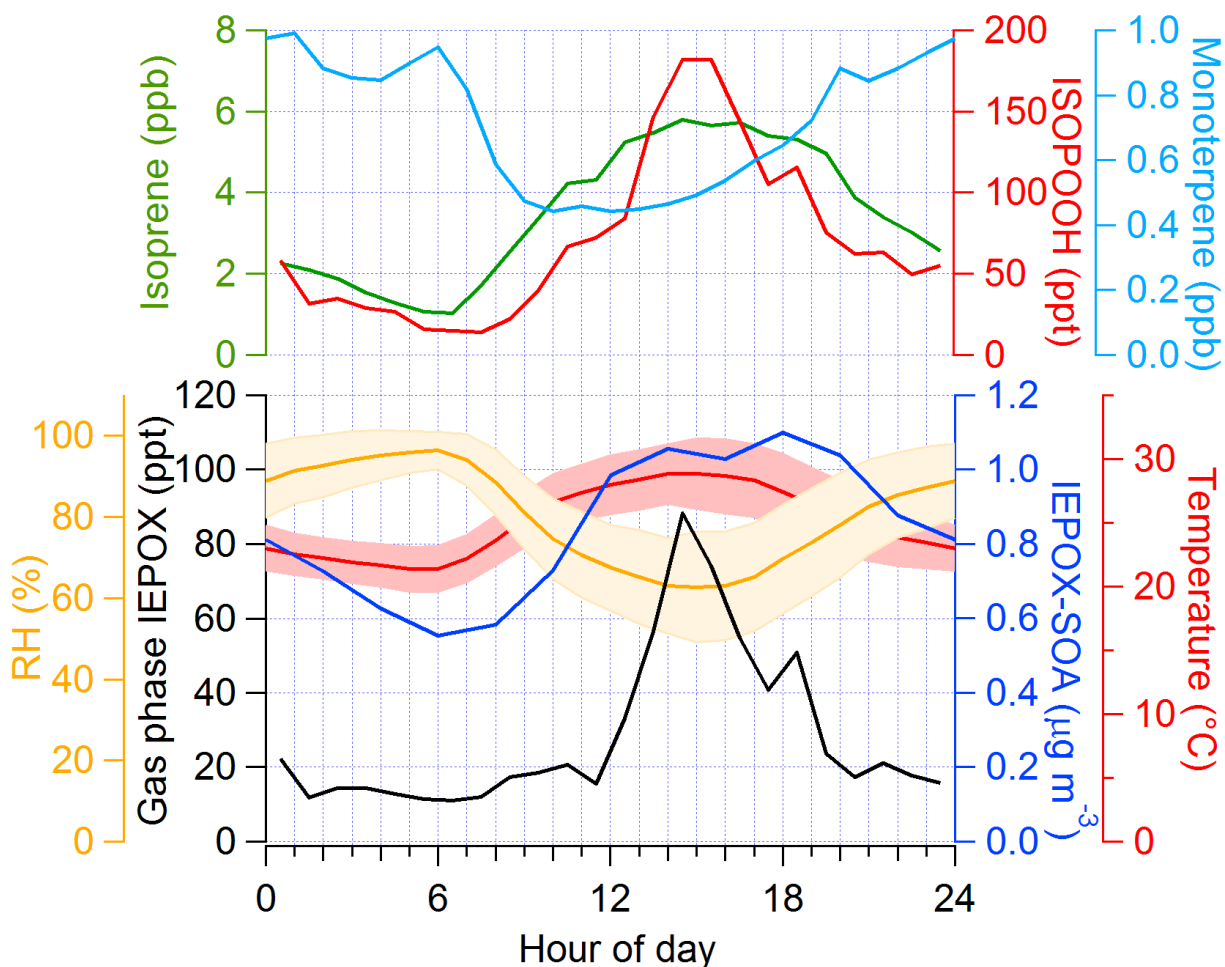
Figure S1. Ambient diurnal cycles of gas phase isoprene, monoterpenes (on-line GC-MS and PTR-MS), ISOPOOH (CF_3O^- CIMS), IEPOX (CF_3O^- CIMS), aerosol phase IEPOX-SOA (AMS), temperature and RH measured in SE US study. The shaded areas of temperature and RH refer to the standard deviation of the averaged value. ISOPOOH and IEPOX were measured by CF_3O^- CIMS from the Wennberg group at Caltech. Isoprene and monoterpene were measured by on-line GC-MS and PTR-MS. These diurnal cycle have also been reported in Hu et al. (2015) and Krechmer et al. (2015).

232

233

234

235

Figure S2. Schematic of the sampling setup in the SE US study. CO gas (~2 ppm before June 27 and ~1ppm after June 28, corresponding to OH reactivity ~10 s^{-1} and 5 s^{-1}, respectively) was injected into the OFR to provide further quantitative constraints on the OH exposure by measuring its decay due to reaction with OH radicals. In our setup, the OFR were sampled the ambient air directly without treatment, while TD were sampled the aerosol through a nafion dryer to RH~40-50%. Before being sampled into aerosol and gas measurement instrumetns, aerosol and gas were dried to RH below 30%.

243

244

Flow reactor shield to protect from rain and heating by direct sunlight

One of the CO injection ports

Ambient air in

Ambient air in through holes

Flow reactor body

Figure S3. Experimental setup for the two OFRs used during SE US study. The reactor on the left was used for the OH-OFR and OH exposure measurements. The right reactor was used to examine O_3 and NO_3 oxidation chemistry. Two reactors were aligned so that the inlet pointed towards the prevailing wind direction.

250

251
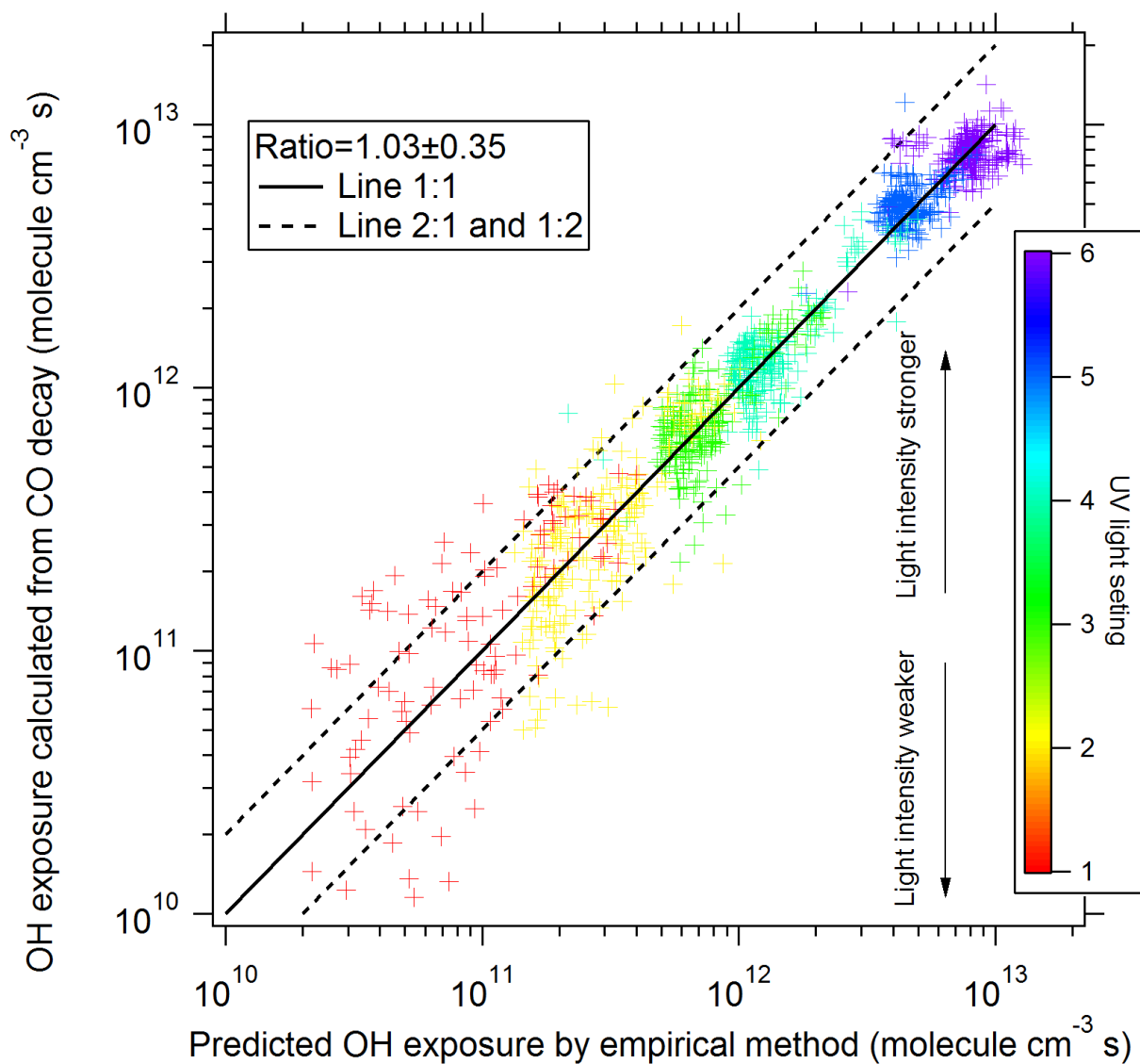
Figure S4. Scatter plot between the OH exposure estimated from the decay of injected CO
measured in-situ vs. OH exposure estimated with the estimation equation of Li et al.(2015), after
calibration to this CO decay dataset. The detailed estimation process of OH exposure in OFR in
SE US study can be seen in Li et al. (2015). The higher scatter at the lowest OH exposures is
caused by the uncertainty of the small CO decay under these conditions.

257

258
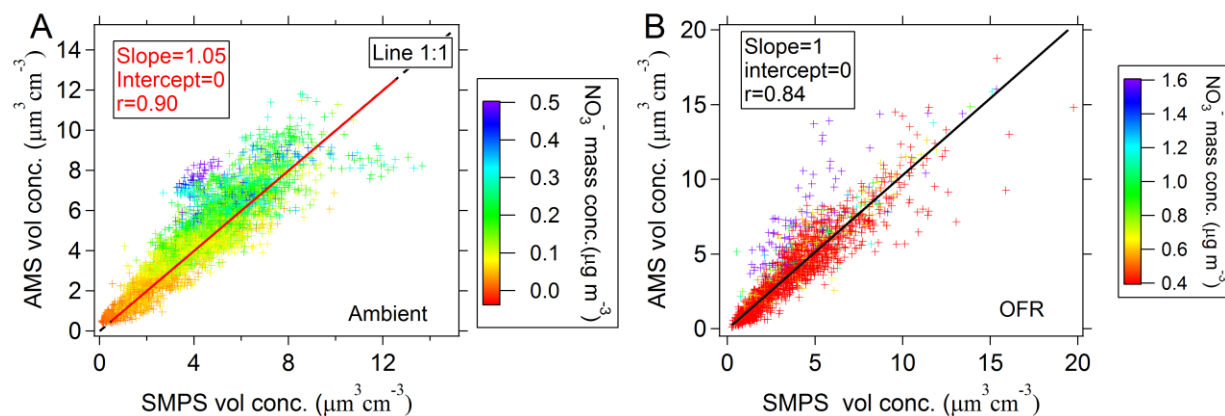
Figure S5. Scatter plots of volume concentrations between AMS and SMPS for ambient air and OFR output during SE US. For points with higher ammonium nitrate concentrations the AMS volume may be higher than the SMPS volume due to evaporation of this species in the SMPS (Khlystov et al., 1996; Palm et al., 2016)
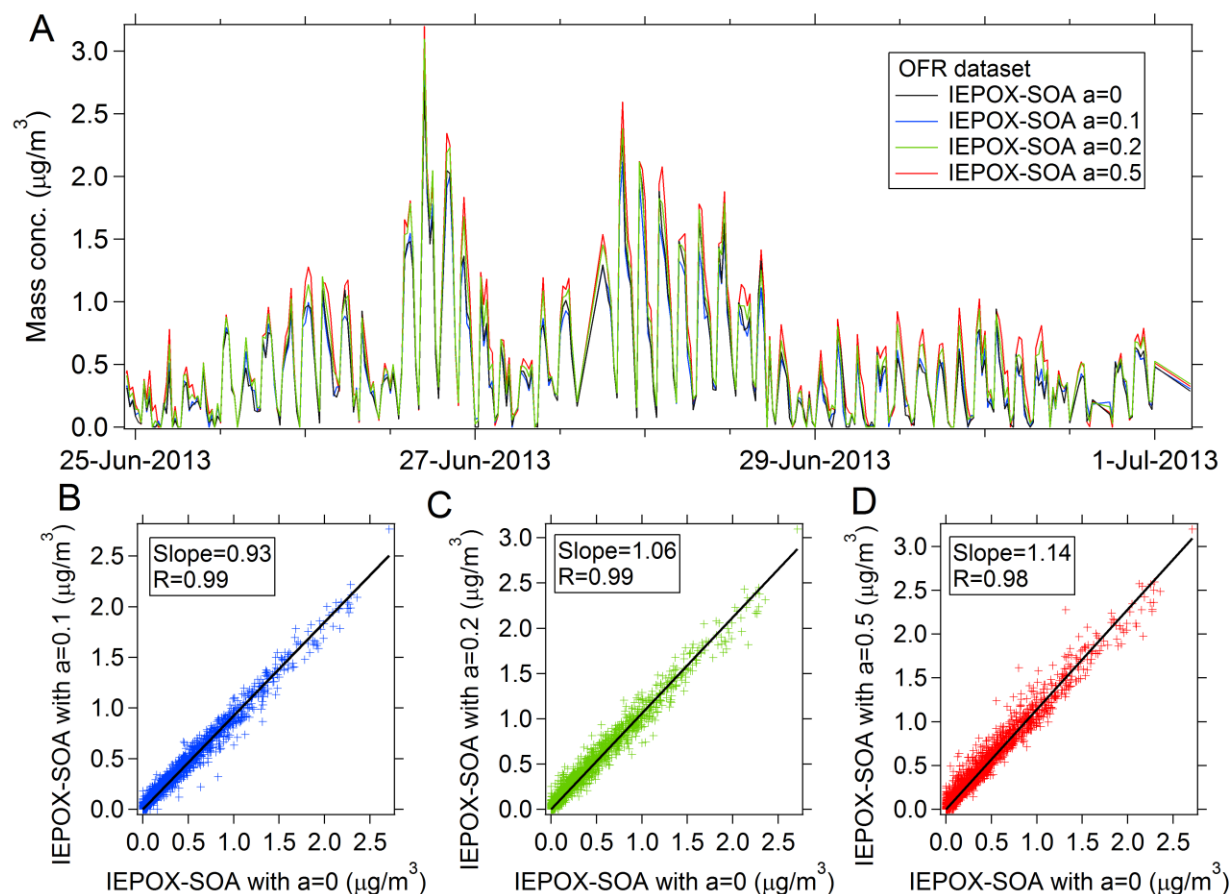
Figure S6. (a) Time series of IEPOX-SOA factors in OH OFR output resolved with ME-2 for different values of the *a* parameter. The *a* parameter controls how strongly one of the factor spectra solved for using ME-2 must resemble the ambient IEPOX-SOA spectrum determined from unconstrained PMF of the ambient data. To allow for visual comparison of the time variations in sufficient detail, only part of the time series of IEPOX-SOA is shown here. Scatter plots of ME-2 resolved IEPOX-SOA factor at *a*-values of (b) 0.1; (c) 0.2; (d) 0.5 vs that factor at *a*-value=0 (fully constrained). Results from entire campaign data are shown in the scatter plots.

273
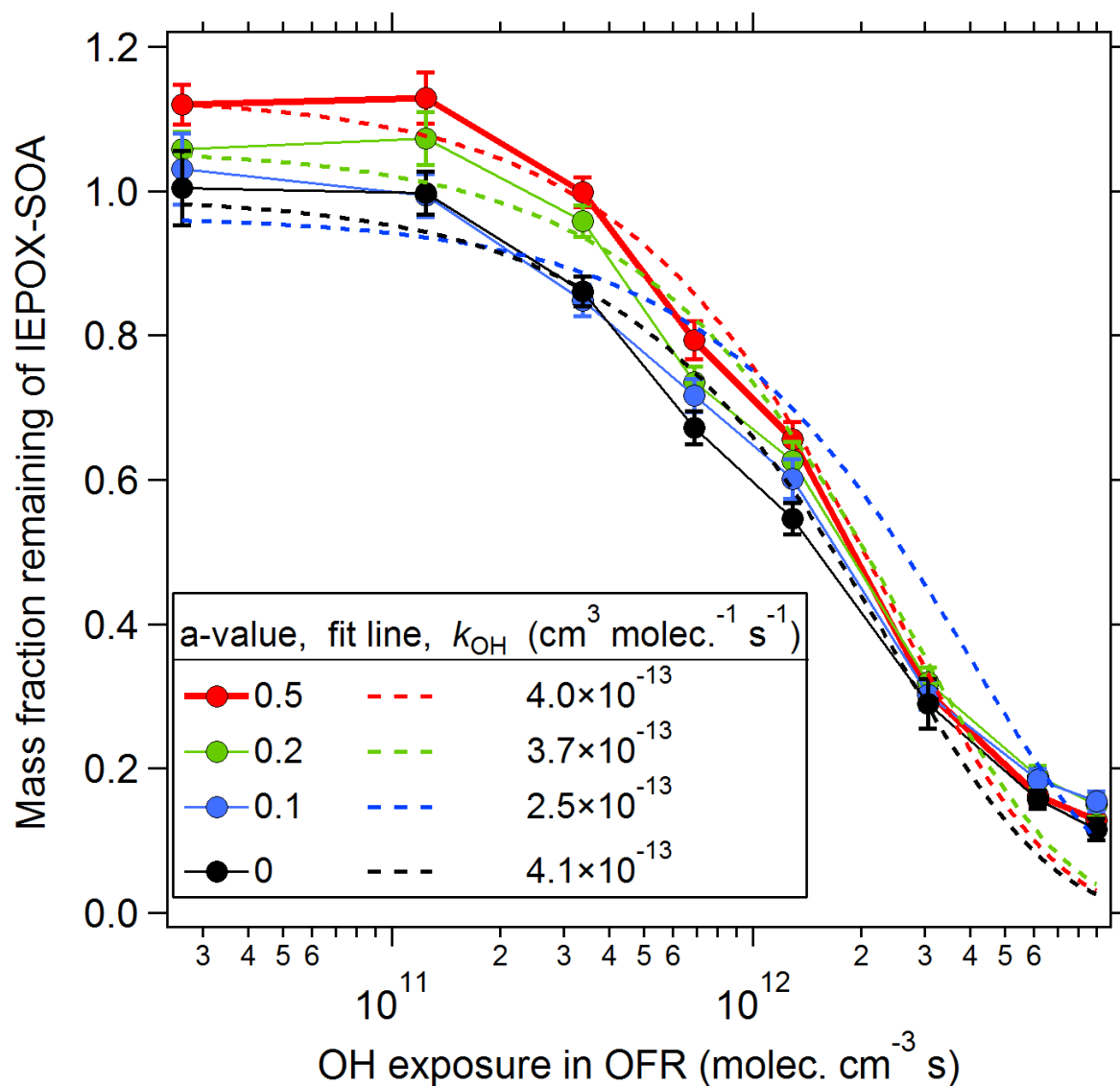
Figure S7. Mass fraction remaining of IEPOX-SOA for different *a*-values in ME-2 as a function
of OH exposures. Error bars shown are standard error of the mean for each quantile.

276
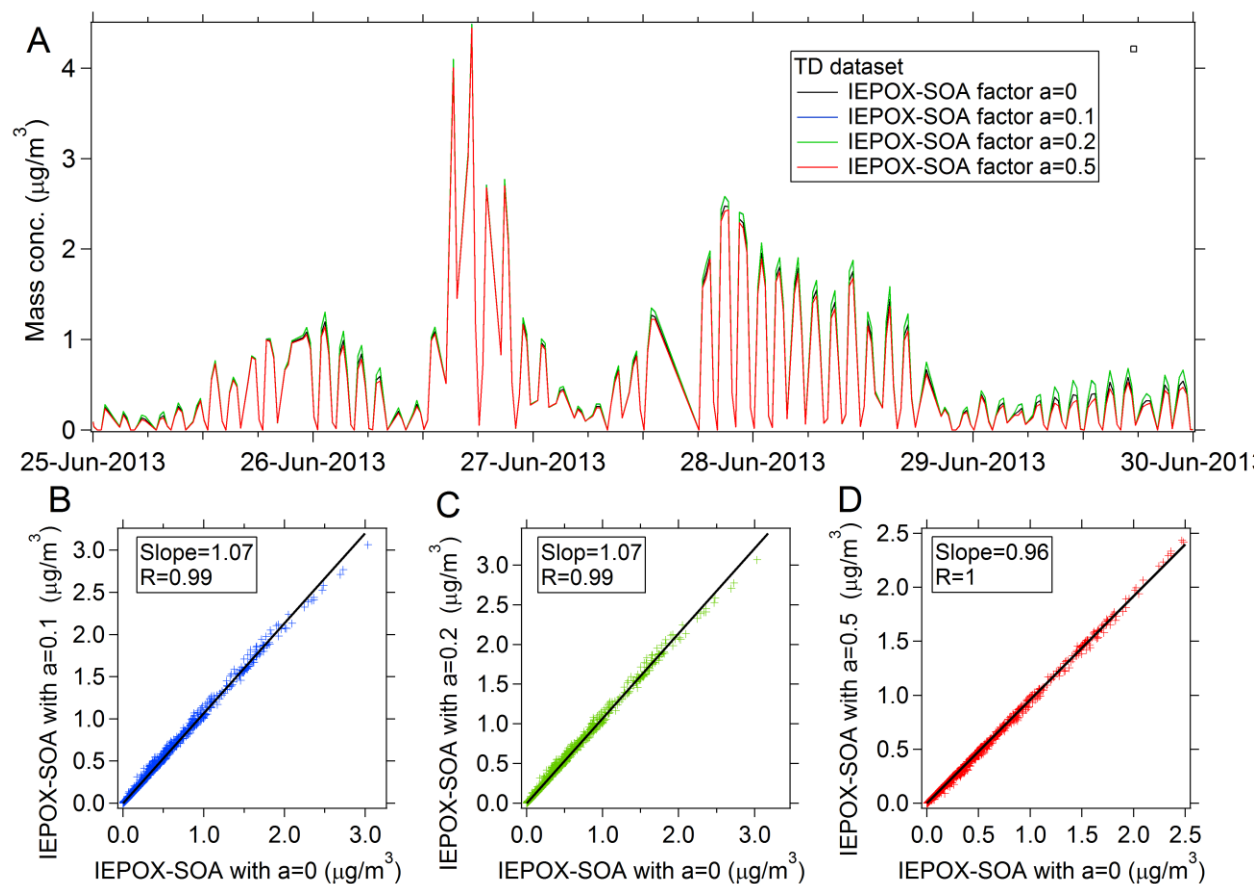
Figure S8. (a) Time series of ME-2 resolved IEPOX-SOA factors at different *a*-values in the thermal denuder (TD) dataset. To allow for visual comparison of the time series, only part of the time period is shown. Scatter plots of ME-2 resolved IEPOX-SOA factor at *a*-values of (b) 0.1; (c) 0.2; (d) 0.5 vs that factor at *a*-value=0 (fully constrained). Results from entire campaign data are shown in the scatter plots.
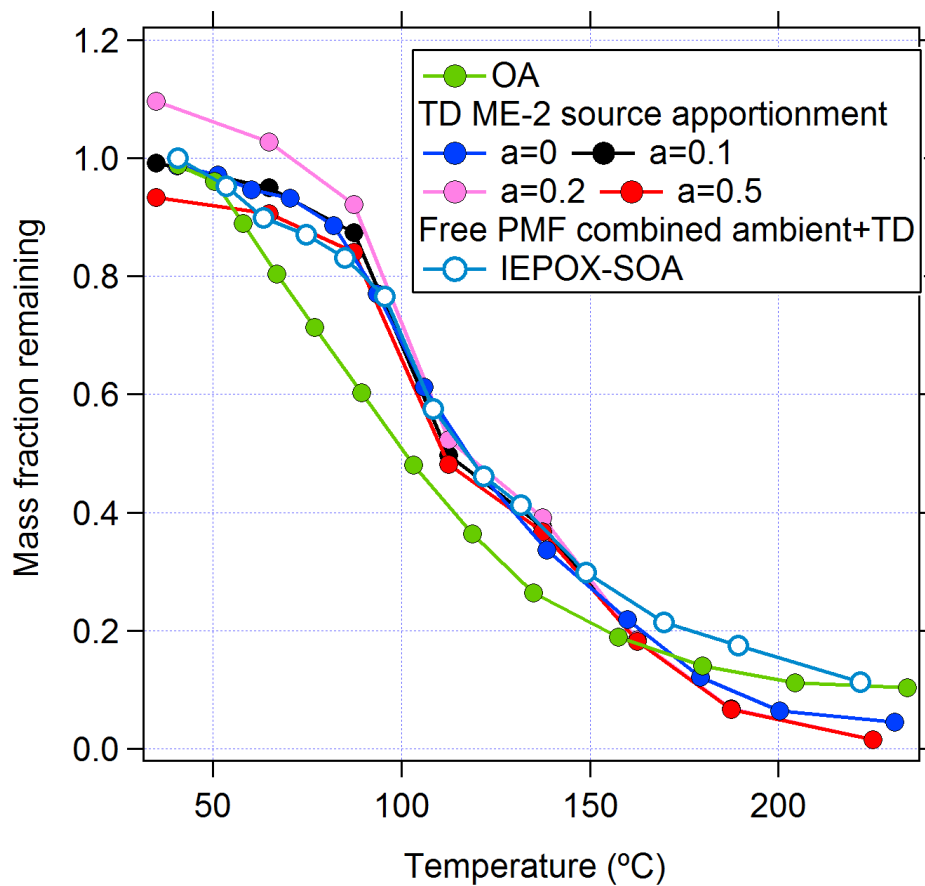
Figure S9. Thermogram comparisons of IEPOX-SOA from constrained ME-2 source apportionment for different *a*-values and unconstrained PMF source apportionment method when performed on the combined ambient+TD dataset. The thermogram of OA is shown for comparison.

290

291
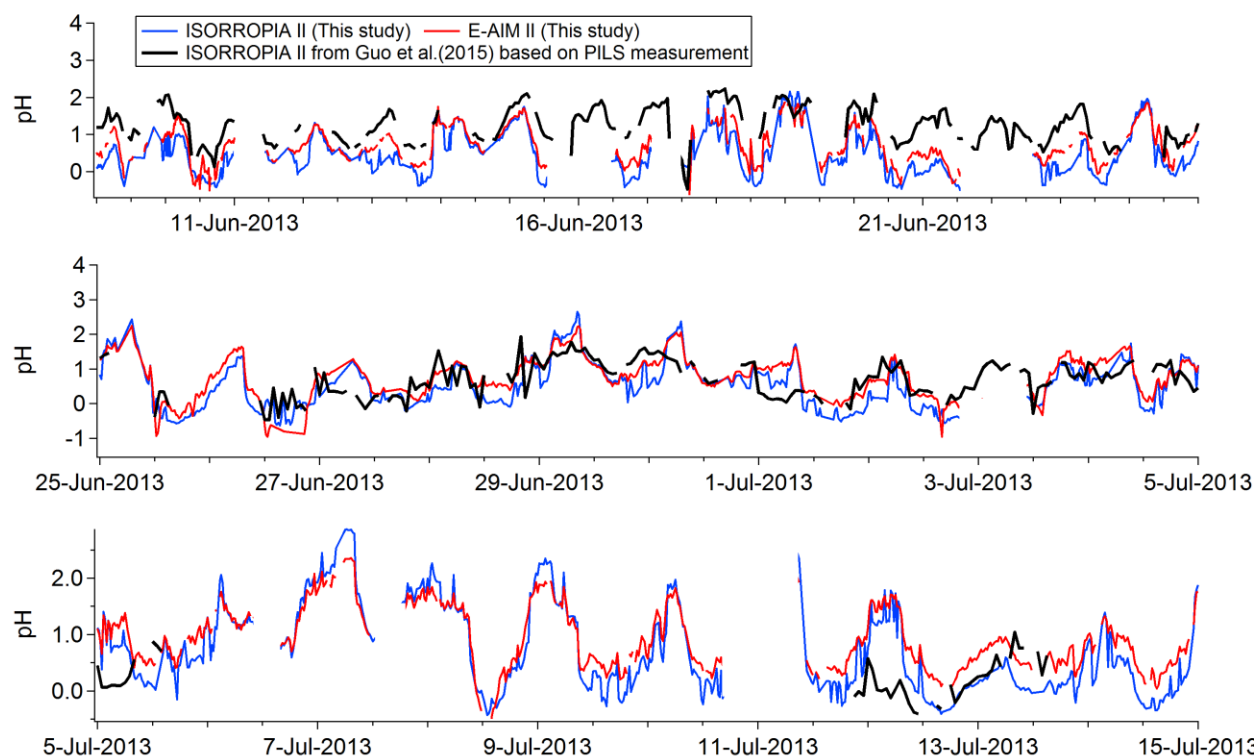
Figure S10. Time series of ambient pH calculated using the ISORROPIA II and E-AIM II models. Metastable condition and forward mode were used in both models. Particle phase NH_4, inorganic NO_3, SO_4 and Cl and gas-phase NH_3 and HNO_3 were used as inputs of the model. The aerosol species were measured by AMS and the gas-phase NH_3 (Saylor et al., 2010) and HNO_3 (Arnold et al., 2007) species were measured by the standard suite of instruments of the SEARCH network site. Average ambient pH over SE US study is 0.8±0.5 from E-AIM II. pH calculated from Guo et al. (2015) is shown here for comparison.

299

300
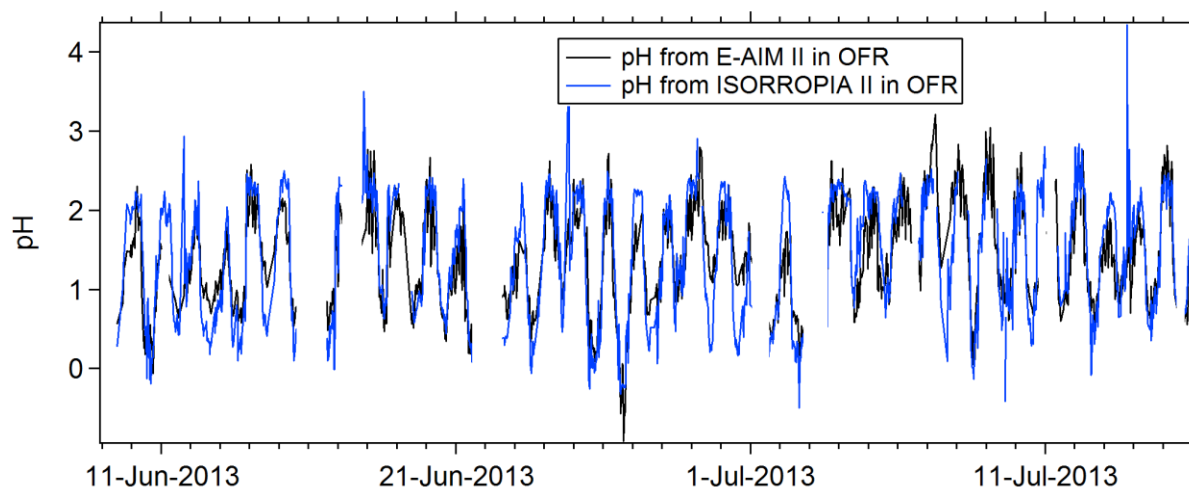
Figure S11. Time series of pH of OFR output aerosol calculated with the ISORROPIA II (Fountoukis and Nenes, 2007) and E-AIM II models (Wexler and Clegg, 2002). Metastable condition and forward mode were used in both models. Particle phase NH_4, inorganic NO_3, SO_4 and Cl in OFR output were measured by our AMS. Ambient gas phase NH_3 and HNO_3 were measured by other instruments at SEARCH. HNO_3 in OFR output was calculated as the sum of ambient HNO_3 plus all ambient NO and NO_2 since the latter two are quickly oxidized to be HNO_3 in OH-OFR (Peng et al., 2015). NH_3 in OFR output was assumed to be the same as in ambient air.
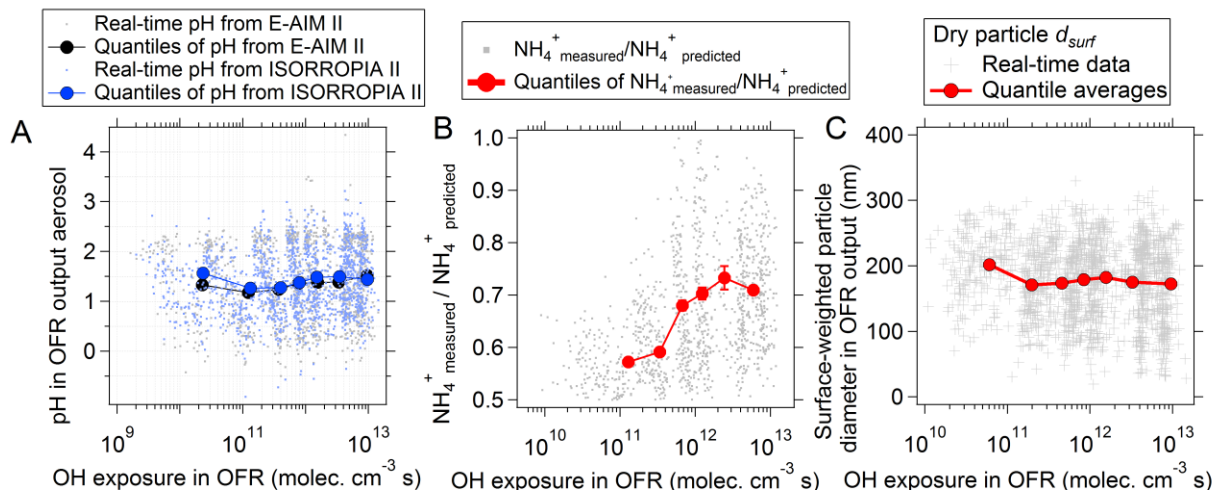
312

Figure S12. (a) Estimated pH in OFR output aerosol from the E-AIM II (Wexler and Clegg, 2002) and ISORROPIA II (Fountoukis and Nenes, 2007) inorganic aerosol models, as a function of OH exposure. The average *pH* in OFR output during SE US study is estimated as 1.35±0.5 from E-AIM II and 1.39±0.7 from ISORROPIA II. (b) Ratio between measured NH_4^+ and NH_4^+ needed to fully neutralize the measured inorganic anions ("predicted") in OFR output air as a function of OH exposure. (c) Dry surface-area weighed diameters (d_{surf}) calculated from SMPS measurement as a function of OH exposure in the OFR. d_{surf} was calculated as particle volume/surface area×6. The average dry d_{surf} over the entire sampling period was calculated to be 190±60 nm. By applying the average particle size growth factor of 1.5 calculated from average kappa (0.27) and ambient RH (Nguyen et al., 2014b), the average d_{surf} for ambient particles is estimated as 282±90 nm; Error bars shown are standard error of the mean for each quantile.
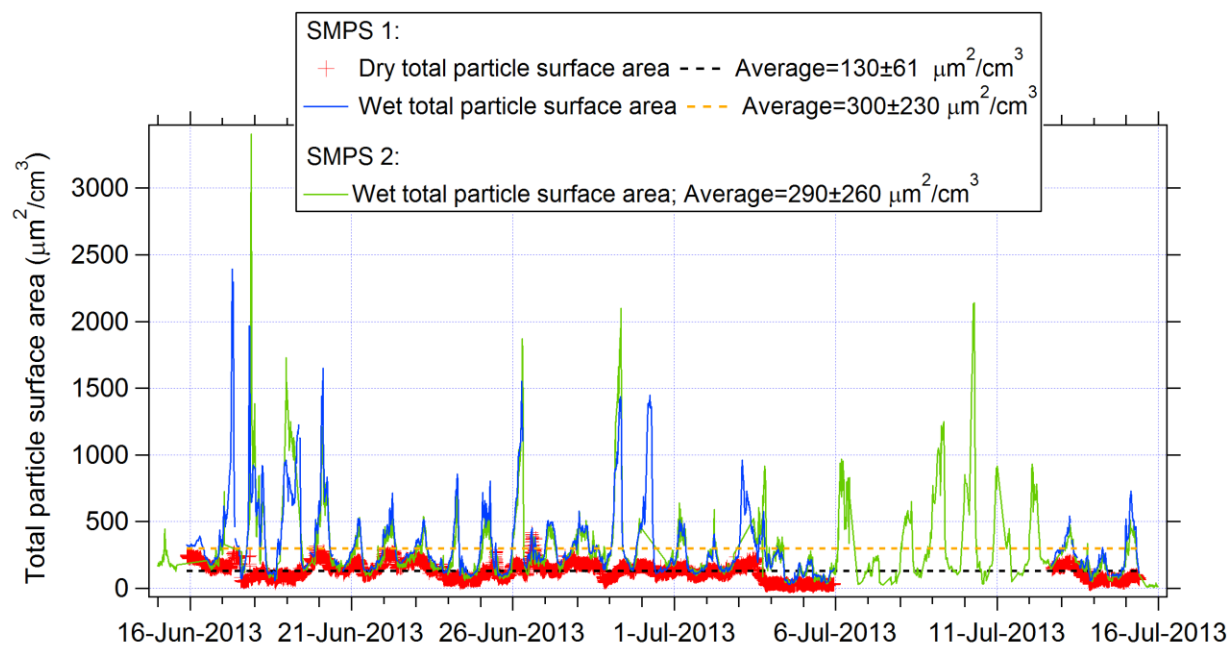
325

326

327

Figure S13. Time series of ambient total dry and wet particle surface area during SE US study. The dry particle surface area was calculated based on SMPS number size distributions. The wet particle surface area was calculated by applying square growth factor to dry particle surface area. The ambient growth factor was estimated based on ambient average kappa (0.27) and real ambient RH (Rissler et al., 2006; Nguyen et al., 2014b). Two CU SMPS are used in SE US study. SMPS 1 sampled ambient aerosol all the time. SMPS 2 sampled in parallel with the AMS and was multiplexed between sampling ambient, the OFR outflows and TD outflow.
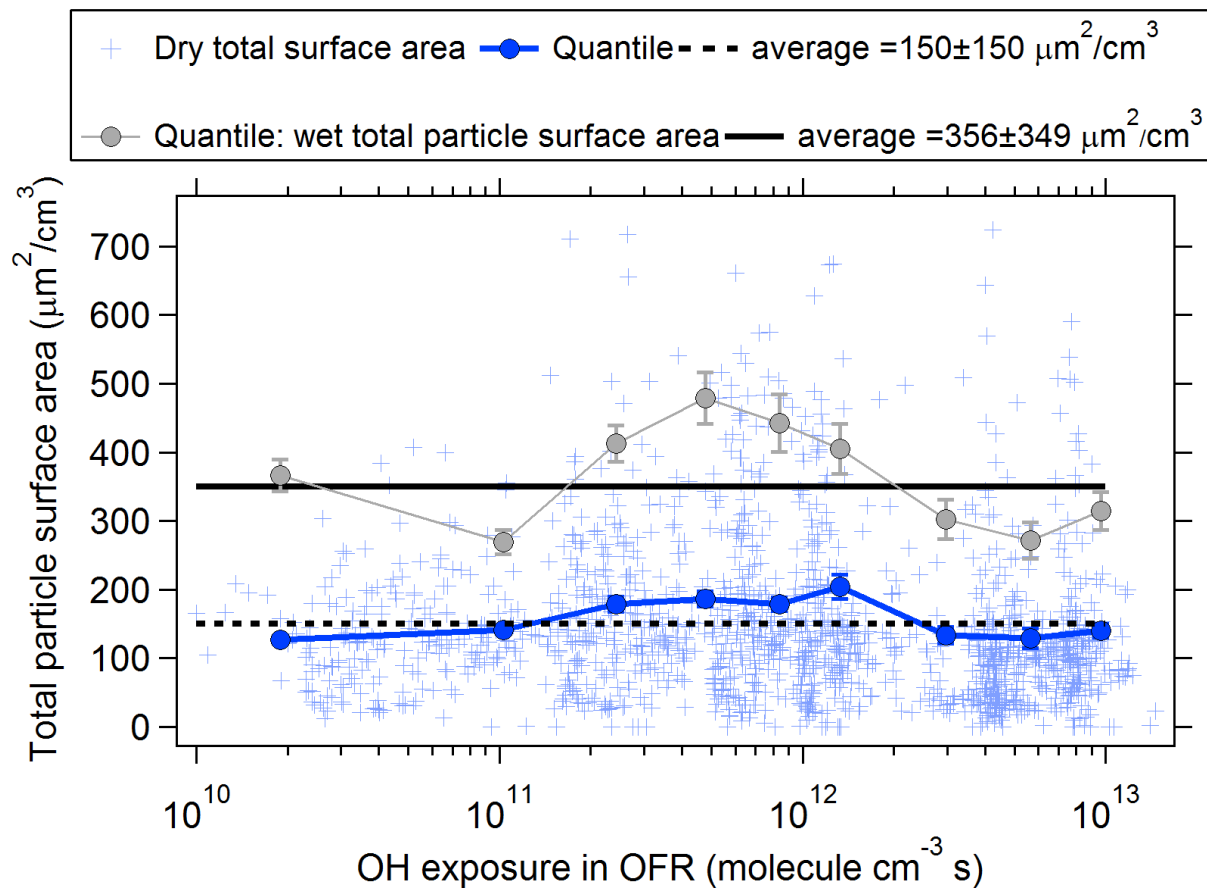
335

Figure S14. Total particle dry and wet surface area (from SMPS measurements) as a function of OH exposure in OFR. Error bars are standard errors of the mean for each quantile.
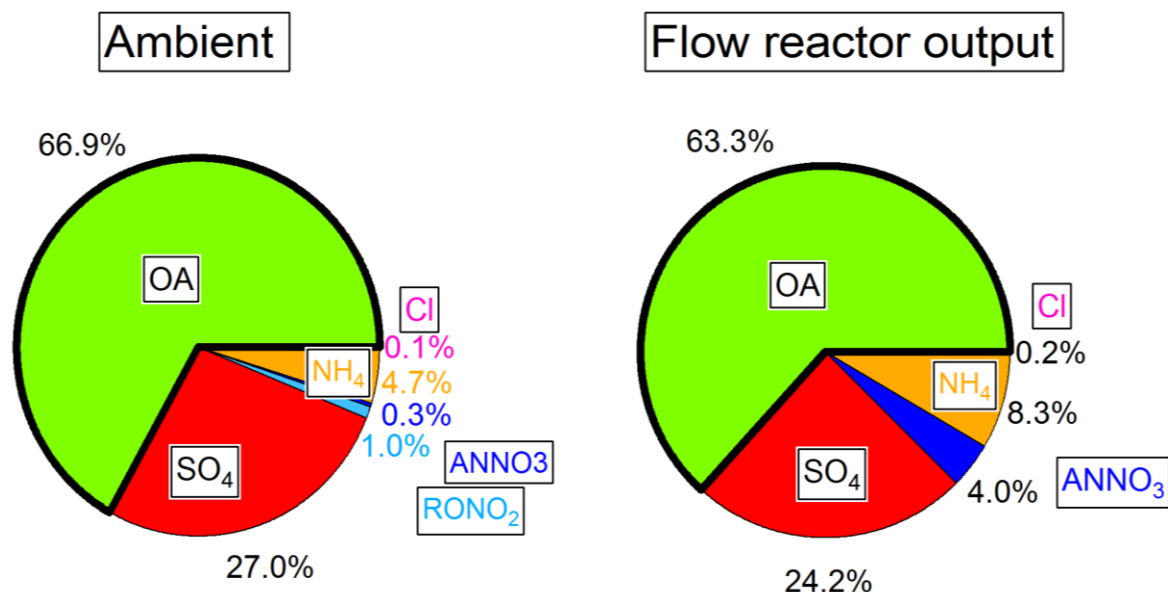
Figure S15. Average composition of submicron non-refractory aerosol measured by AMS of ambient and OFR output during SE US study. The OFR output is averaged over all OH exposures. $ANNO_3$ represents nitrate that is part of ammonium nitrate, while $RONO_2$ represents nitrate that is organic in nature (See e.g., Ayres et al., 2015). The slightly lower OA fraction in OFR output is mainly caused by the fragmentation and volatilization of OA at high OH exposures ($>10^{12}$ molec. cm^{-3} s); see example shown in Fig. 6b. An empirical method based on O/C and H/C (0.65 and 1.56 in average, respectively) ratios was used to calculate the ambient OA density (1.34 ± 0.4) (Kuwata et al., 2012);
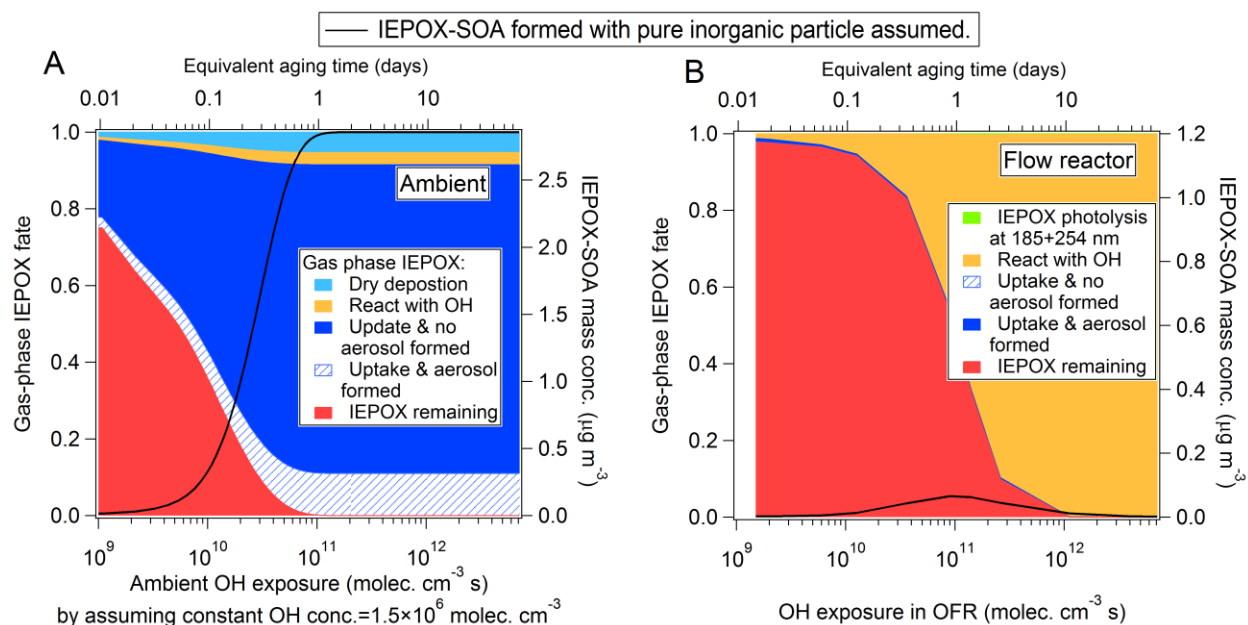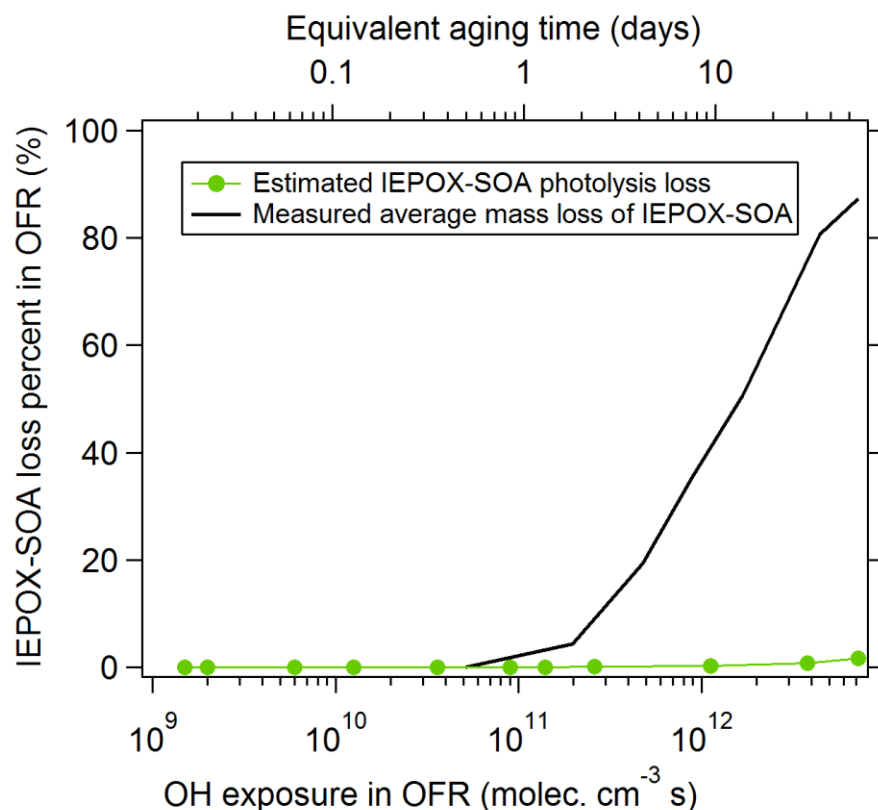
353

354

Figure S16. IEPOX fate (a) for the ambient and (b) flow reactor conditions calculated by the model under the pure inorganic aerosol scenario.

358

359

360

Figure S17. Estimated IEPOX-SOA losses due to photolysis inside the OFR at 185 and 254 nm, as a function of OH exposure. Results show negligible importance of photolysis compared to the observed loss of IEPOX-SOA in the OFR. Absorption cross section data is obtained (254 nm) or estimated (185 nm) from Lin et al. (2014) from acidified $(NH_4)_2SO_4$ particles. Quantum yield=1 was assumed here to obtain an upper limit of the photolysis fraction. The photon fluxes of 185 and 254 nm used here range between 5×10^9-3×10^{13} photon cm^{-2} s^{-1} and 1×10^{12}-3×10^{15} photon cm^{-2} s^{-1}, respectively.
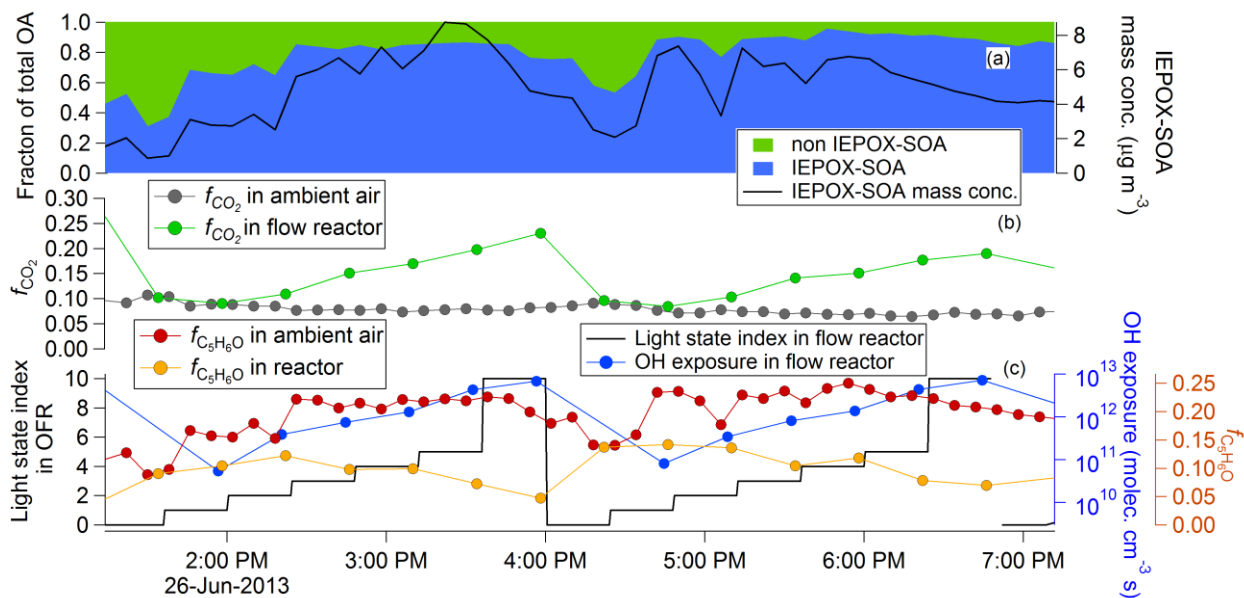
368

369

27

370

Figure S18. Composition of ambient OA and of OFR output OA during a period with very high IEPOX-SOA/OA ratio in SE US study. (a) IEPOX-SOA mass concentration and the IEPOX-SOA fraction of OA in ambient air. (b) Time series of f_{CO_2} of OA in ambient air and OFR outflow. (c) OH exposure in the OFR and UV light intensity index (with zero corresponding to no light, and light intensity increasing with the index), and $f_{C_5H_6O}$ in ambient and reactor air. During this IEPOX-SOA-dominated period, 80−90% of ambient OA was IEPOX-SOA. The data from 2:00-7:00 pm in this figure was used to calculate the mass fraction remaining of IEPOX-SOA, $C_5H_6O^+$ and OA in Fig. S19.

379

380

381
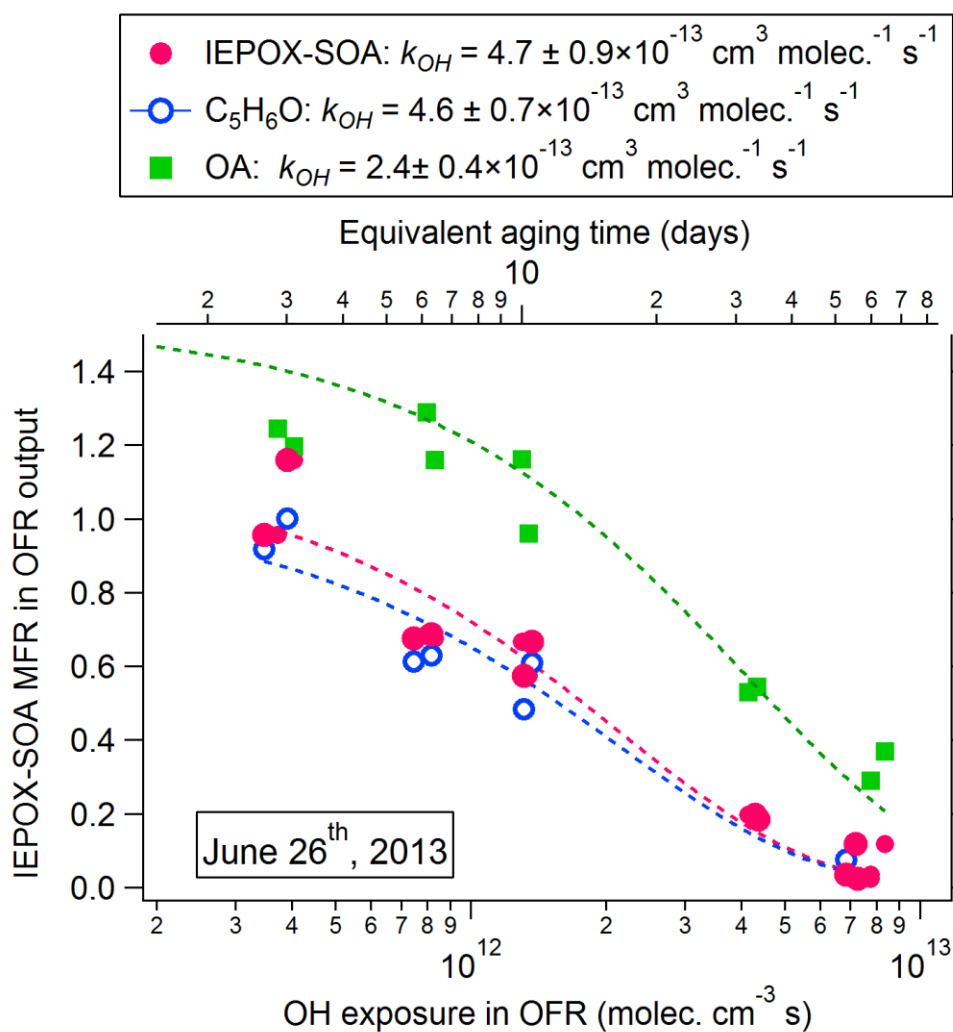
Figure S19. Mass fraction remaining of IEPOX-SOA, $C_5H_6O^+$ and OA as a function of OH exposure during a period when 80-90% ambient OA at the SE US CRT Supersite was composed of IEPOX-SOA on June 26th, 2013, as illustrated by Fig. S18. k_{OH} are shown in the legend with fitting parameter uncertainties. Note that OA in the OFR outflow is larger than ambient OA at lower OH exposures due to SOA formation in the OFR.

382

383

384

385

386

387

388

389

390

391

Figure S21 Fraction of IEPOX-SOA remaining in OFR output as a function of OH exposure during the GoAmazon2014/5 study. Datapoints are color-coded by ambient RH.
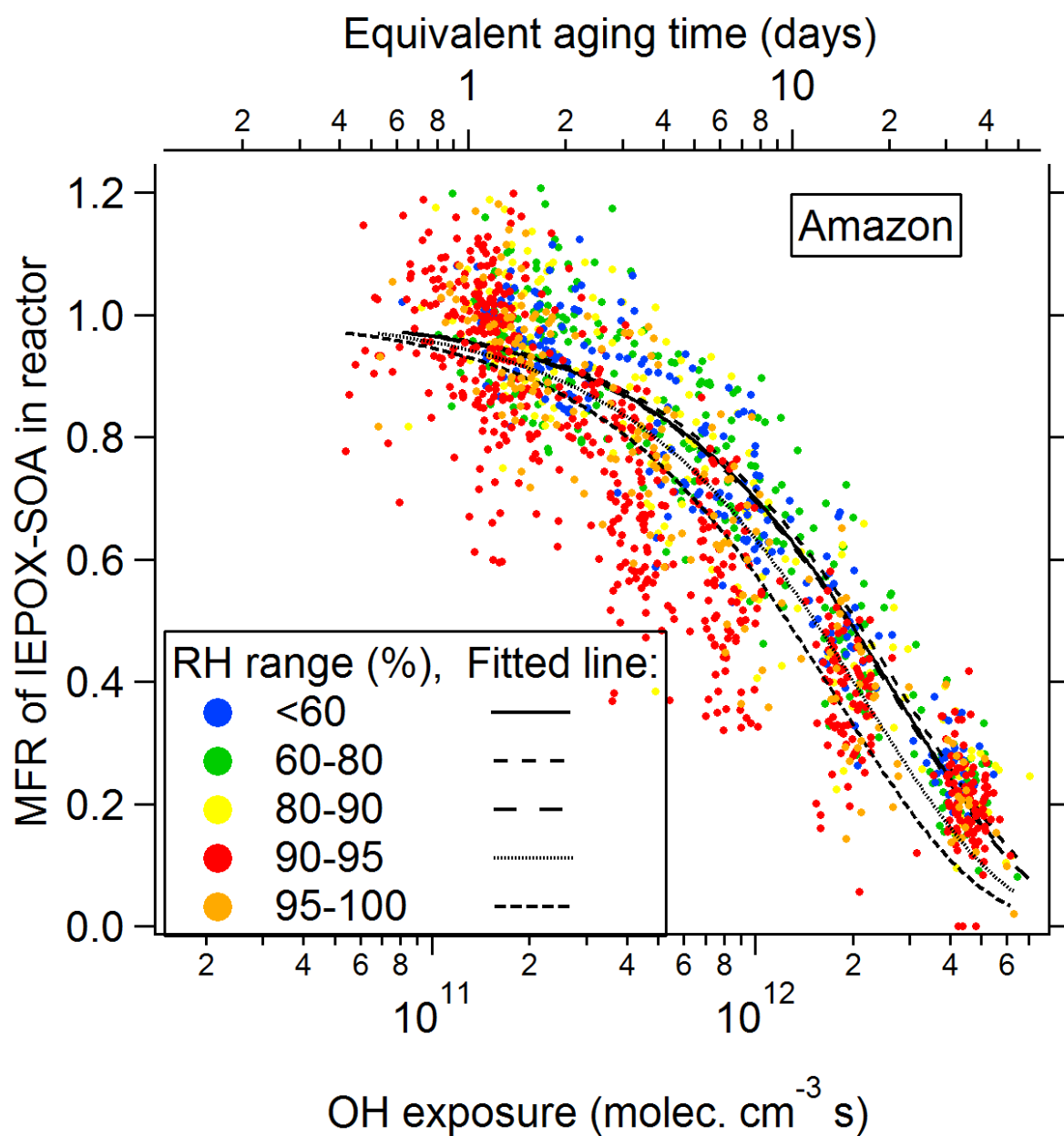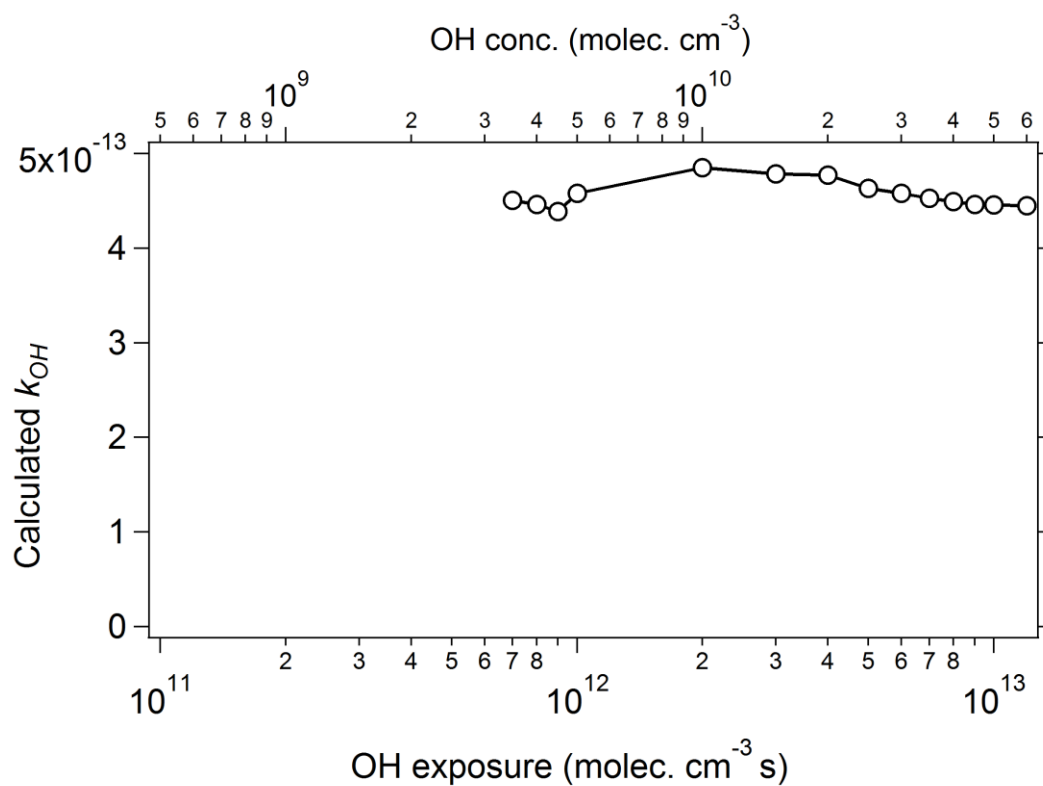
398

Figure S22 Calculated k_{OH} for different OH exposure levels. Each point represents the calculated k_{OH} using only datapoints below the corresponding y-axis OH exposure value.

References

Aiken, A. C., Decarlo, P. F., Kroll, J. H., Worsnop, D. R., Huffman, J. A., Docherty, K. S., Ulbrich, I. M., Mohr, C., Kimmel, J. R., Sueper, D., Sun, Y., Zhang, Q., Trimborn, A., Northway, M., Ziemann, P. J., Canagaratna, M. R., Onasch, T. B., Alfarra, M. R., Prevot, A. S. H., Dommen, J., Duplissy, J., Metzger, A., Baltensperger, U., and Jimenez, J. L.: O/C and OM/OC ratios of primary, secondary, and ambient organic aerosols with high-resolution time-of-flight aerosol mass spectrometry, Environ. Sci. Technol., 42, 4478-4485, Doi 10.1021/Es703009q, 2008.

Arnold, J. R., Hartsell, B. E., Luke, W. T., Rahmat Ullah, S. M., Dasgupta, P. K., Greg Huey, L., and Tate, P.: Field test of four methods for gas-phase ambient nitric acid, Atmos. Environ., 41, 4210-4226, 2007.

Atkinson, R., and Arey, J.: Gas-phase tropospheric chemistry of biogenic volatile organic compounds: a review, Atmos. Environ., 37, 197-219, 2003.

Ayres, B. R., Allen, H. M., Draper, D. C., Brown, S. S., Wild, R. J., Jimenez, J. L., Day, D. A., Campuzano-Jost, P., Hu, W., de Gouw, J., Koss, A., Cohen, R. C., Duffey, K. C., Romer, P., Baumann, K., Edgerton, E., Takahama, S., Thornton, J. A., Lee, B. H., Lopez-Hilfiker, F. D., Mohr, C., Wennberg, P. O., Nguyen, T. B., Teng, A., Goldstein, A. H., Olson, K., and Fry, J. L.: Organic nitrate aerosol formation via NO3 + biogenic volatile organic compounds in the southeastern United States, Atmos. Chem. Phys., 15, 13377-13392, 10.5194/acp-15-13377-2015, 2015.

Bates, K. H., Crounse, J. D., St. Clair, J. M., Bennett, N. B., Nguyen, T. B., Seinfeld, J. H., Stoltz, B. M., and Wennberg, P. O.: Gas Phase Production and Loss of Isoprene Epoxydiols, J. Phys. Chem. A, 118, 1237-1246, 10.1021/jp4107958, 2014.

Bates, K. H., Nguyen, T. B., Teng, A. P., Crounse, J. D., Kjaergaard, H. G., Stoltz, B. M., Seinfeld, J. H., and Wennberg, P. O.: Production and Fate of C4 Dihydroxycarbonyl Compounds from Isoprene Oxidation, J. Phys. Chem. A, 120, 106–117, 10.1021/acs.jpca.5b10335, 2015.

Canagaratna, M. R., Jimenez, J. L., Kroll, J. H., Chen, Q., Kessler, S. H., Massoli, P., Hildebrandt Ruiz, L., Fortner, E., Williams, L. R., Wilson, K. R., Surratt, J. D., Donahue, N. M., Jayne, J. T., and Worsnop, D. R.: Elemental ratio measurements of organic compounds using aerosol mass spectrometry: characterization, improved calibration, and implications, Atmos. Chem. Phys., 15, 253-272, 10.5194/acp-15-253-2015, 2015.

Canonaco, F., Crippa, M., Slowik, J. G., Baltensperger, U., and Prévôt, A. S. H.: SoFi, an IGOR-based interface for the efficient use of the generalized multilinear engine (ME-2) for the source apportionment: ME-2 application to aerosol mass spectrometer data, Atmos. Meas. Tech., 6, 3649-3661, 10.5194/amt-6-3649-2013, 2013.

Chen, H., Karion, A., Rella, C. W., Winderlich, J., Gerbig, C., Filges, A., Newberger, T., Sweeney, C., and Tans, P. P.: Accurate measurements of carbon monoxide in humid air using the cavity ring-down spectroscopy (CRDS) technique, Atmos. Meas. Tech., 6, 1031-1040, 10.5194/amt-6-1031-2013, 2013.

CreĠu, G.: Searching for new solutions humidity measurements in the environments, J Electr. Electro. Engineer., 1, 41-45, 2008.

DeCarlo, P. F., Kimmel, J. R., Trimborn, A., Northway, M. J., Jayne, J. T., Aiken, A. C., Gonin, M., Fuhrer, K., Horvath, T., Docherty, K. S., Worsnop, D. R., and Jimenez, J. L.: Field-deployable, high-resolution, time-of-flight aerosol mass spectrometer, Anal. Chem., 78, 8281-8289, Doi 10.1021/Ac061249n, 2006.

Fleming, G., Anderson, M. M., Harrison, A. J., and Pickett, L. W.: Effect of Ring Size on the Far Ultraviolet Absorption and Photolysis of Cyclic Ethers, J. Phys. Chem. A, 30, 351-354, 10.1063/1.1729951, 1959.

448 Fountoukis, C., and Nenes, A.: ISORROPIA II: a computationally efficient thermodynamic equilibrium
449   model for K^+–Ca^{2+}–Mg^{2+}–NH_4^+–Na^+–SO_4^{2-}–NO_3^-–Cl^-–H_2O aerosols, Atmos. Chem. Phys., 7,
450   4639-4659, 10.5194/acp-7-4639-2007, 2007.
451 Gaston, C. J., Riedel, T. P., Zhang, Z., Gold, A., Surratt, J. D., and Thornton, J. A.: Reactive Uptake of an
452   Isoprene-Derived Epoxydiol to Submicron Aerosol Particles, Environ. Sci. Technol., 48,
453   11178−11186, 10.1021/es5034266, 2014.
454 Guo, H., Xu, L., Bougiatioti, A., Cerully, K. M., Capps, S. L., Hite Jr, J. R., Carlton, A. G., Lee, S. H.,
455   Bergin, M. H., Ng, N. L., Nenes, A., and Weber, R. J.: Fine-particle water and pH in the
456   southeastern United States, Atmos. Chem. Phys., 15, 5211-5228, 10.5194/acp-15-5211-2015,
457   2015.
458 Hennigan, C. J., Izumi, J., Sullivan, A. P., Weber, R. J., and Nenes, A.: A critical evaluation of proxy
459   methods used to estimate the acidity of atmospheric particles, Atmos. Chem. Phys., 15, 2775-
460   2790, 10.5194/acp-15-2775-2015, 2015.
461 Hu, W. W., Campuzano-Jost, P., Palm, B. B., Day, D. A., Ortega, A. M., Hayes, P. L., Krechmer, J. E.,
462   Chen, Q., Kuwata, M., Liu, Y. J., de Sá, S. S., McKinney, K., Martin, S. T., Hu, M.,
463   Budisulistiorini, S. H., Riva, M., Surratt, J. D., St. Clair, J. M., Isaacman-Van Wertz, G., Yee, L.
464   D., Goldstein, A. H., Carbone, S., Brito, J., Artaxo, P., de Gouw, J. A., Koss, A., Wisthaler, A.,
465   Mikoviny, T., Karl, T., Kaser, L., Jud, W., Hansel, A., Docherty, K. S., Alexander, M. L.,
466   Robinson, N. H., Coe, H., Allan, J. D., Canagaratna, M. R., Paulot, F., and Jimenez, J. L.:
467   Characterization of a real-time tracer for isoprene epoxydiols-derived secondary organic aerosol
468   (IEPOX-SOA) from aerosol mass spectrometer measurements, Atmos. Chem. Phys., 15, 11807-
469   11833, 10.5194/acp-15-11807-2015, 2015.
470 Huffman, J. A., Docherty, K. S., Aiken, A. C., Cubison, M. J., Ulbrich, I. M., DeCarlo, P. F., Sueper, D.,
471   Jayne, J. T., Worsnop, D. R., Ziemann, P. J., and Jimenez, J. L.: Chemically-resolved aerosol
472   volatility measurements from two megacity field studies, Atmos Chem Phys, 9, 7161-7182, 2009.
473 Jiménez, E., Lanza, B., Antiñolo, M., and Albaladejo, J.: Photooxidation of Leaf-Wound Oxygenated
474   Compounds, 1-Penten-3-ol, (Z)-3-Hexen-1-ol, and 1-Penten-3-one, Initiated by OH Radicals and
475   Sunlight, Environ. Sci. Technol., 43, 1831-1837, 10.1021/es8027814, 2009.
476 Johnson, T., Capel, J., and Ollison, W.: Measurement of microenvironmental ozone concentrations in
477   Durham, North Carolina, using a 2B Technologies 205 Federal Equivalent Method monitor and
478   an interference-free 2B Technologies 211 monitor, J. Air Waste Manage, 64, 360-371,
479   10.1080/10962247.2013.839968, 2014.
480 Jorand, F., Kerhoas, L., Heiss, A., Einhorn, J., and Sahetchian, K.: Determination of the ultra violet
481   absorption cross section of hexyl-ketohydroperoxides in solution in acetonitrile, J. photochem.
482   and Photobio. A, 134, 119-125, 2000.
483 Jordan, A., Haidacher, S., Hanel, G., Hartungen, E., Märk, L., Seehauser, H., Schottkowsky, R., Sulzer,
484   P., and Märk, T. D.: A high resolution and high sensitivity proton-transfer-reaction time-of-flight
485   mass spectrometer (PTR-TOF-MS), Int. J. Mass Spectrom., 286, 122-128, 2009.
486 Keller-Rudek, H., Moortgat, G. K., Sander, R., and Sörensen, R.: The MPI-Mainz UV/VIS Spectral Atlas
487   of Gaseous Molecules of Atmospheric Interest, Earth Syst. Sci. Data, 5, 365-373, 10.5194/essd-5-
488   365-2013, 2013.
489 Khlystov, A., Ten Brink, H. M., and Toivonen, A.: Evaporation of ammonium nitrate aerosol in
490   DMPS/SMPS, J. Aerosol. Sci., 27, S75-S76, 1996.
491 Krechmer, J. E., Coggon, M. M., Massoli, P., Nguyen, T. B., Crounse, J. D., Hu, W., Day, D. A., Tyndall,
492   G. S., Henze, D. K., Rivera-Rios, J. C., Nowak, J. B., Kimmel, J. R., Mauldin, R. L., Stark, H.,
493   Jayne, J. T., Sipilä, M., Junninen, H., St. Clair, J. M., Zhang, X., Feiner, P. A., Zhang, L., Miller,
494   D. O., Brune, W. H., Keutsch, F. N., Wennberg, P. O., Seinfeld, J. H., Worsnop, D. R., Jimenez,
495   J. L., and Canagaratna, M. R.: Formation of Low Volatility Organic Compounds and Secondary
496   Organic Aerosol from Isoprene Hydroxyhydroperoxide Low-NO Oxidation, Environ. Sci.
497   Technol., 49 10330–10339, 10.1021/acs.est.5b02031, 2015.

498 Kuwata, M., Zorn, S. R., and Martin, S. T.: Using Elemental Ratios to Predict the Density of Organic
499   Material Composed of Carbon, Hydrogen, and Oxygen, Environ. Sci. Technol., 46, 787–794,
500   10.1021/es202525q, 2012.
501 Lee, S.-H., Murphy, D. M., Thomson, D. S., and Middlebrook, A. M.: Chemical components of single
502   particles measured with Particle Analysis by Laser Mass Spectrometry (PALMS) during the
503   Atlanta SuperSite Project: Focus on organic/sulfate, lead, soot, and mineral particles, J.
504   Geophys. Res., 107, 10.1029/2000jd000011, 2002.
505 Li, R., Palm, B. B., Ortega, A. M., Hlywiak, J. A., Hu, W., Peng, Z., Day, D. A., Knote, C., Brune, W. H.,
506   de Gouw, J. A., and Jimenez, J. L.: Modeling the Radical Chemistry in an Oxidation Flow
507   Reactor: Radical Formation and Recycling, Sensitivities, and OH Exposure Estimation
508   Equation, , J. Phys. Chem. A,, 10.1021/jp509534k, 2015.
509 Liao, J., Froyd, K. D., Murphy, D. M., Keutsch, F. N., Yu, G., Wennberg, P. O., St. Clair, J. M., Crounse,
510   J. D., Wisthaler, A., Mikoviny, T., Jimenez, J. L., Campuzano Jost, P., Day, D. A., Hu, W.,
511   Ryerson, T. B., Pollack, I. B., Peischl, J., Anderson, B. E., Ziemba, L. D., Blake, D. R., Meinardi,
512   S., and Diskin, G.: Airborne measurements of organosulfates over the continental US, , J.
513   Geophys. Res., 120, 2990-3005, 10.1002/2014jd022378, 2015.
514 Lin, Y.-H., Budisulistiorini, S. H., Chu, K., Siejack, R. A., Zhang, H., Riva, M., Zhang, Z., Gold, A.,
515   Kautzman, K. E., and Surratt, J. D.: Light-Absorbing Oligomer Formation in Secondary Organic
516   Aerosol from Reactive Uptake of Isoprene Epoxydiols, Environ. Sci. Technol., 48, 12012-12021,
517   10.1021/es503142b, 2014.
518 Mao, J., Ren, X., Brune, W. H., Olson, J. R., Crawford, J. H., Fried, A., Huey, L. G., Cohen, R. C.,
519   Heikes, B., Singh, H. B., Blake, D. R., Sachse, G. W., Diskin, G. S., Hall, S. R., and Shetter, R.
520   E.: Airborne measurement of OH reactivity during INTEX-B, Atmos. Chem. Phys., 9, 163-173,
521   10.5194/acp-9-163-2009, 2009.
522 Martins, G., Ferreira-Rodrigues, A. M., Rodrigues, F. N., de Souza, G. G. B., Mason, N. J., Eden, S.,
523   Duflot, D., Flament, J. P., Hoffmann, S. V., Delwiche, J., Hubin-Franskin, M. J., and Limao-
524   Vieira, P.: Valence shell electronic spectroscopy of isoprene studied by theoretical calculations
525   and by electron scattering, photoelectron, and absolute photoabsorption measurements, Phys.
526   Chem. Chem. Phys., 11, 11219-11231, 10.1039/b916620c, 2009.
527 Middlebrook, A. M., Bahreini, R., Jimenez, J. L., and Canagaratna, M. R.: Evaluation of Composition-
528   Dependent Collection Efficiencies for the Aerodyne Aerosol Mass Spectrometer using Field
529   Data, Aerosol. Sci. Tech., 46, 258-271, 10.1080/02786826.2011.620041, 2012.
530 Nguyen, T. B., Coggon, M. M., Bates, K. H., Zhang, X., Schwantes, R. H., Schilling, K. A., Loza, C. L.,
531   Flagan, R. C., Wennberg, P. O., and Seinfeld, J. H.: Organic aerosol formation from the reactive
532   uptake of isoprene epoxydiols (IEPOX) onto non-acidified inorganic seeds, Atmos. Chem. Phys.,
533   14, 3497-3510, 10.5194/acp-14-3497-2014, 2014a.
534 Nguyen, T. B., Crounse, J. D., Teng, A. P., St. Clair, J. M., Paulot, F., Wolfe, G. M., and Wennberg, P.
535   O.: Rapid deposition of oxidized biogenic compounds to a temperate forest, , Proc. Natl. Acad.
536   Sci. USA, 112, E392-E401, 10.1073/pnas.1418702112, 2015.
537 Nguyen, T. K. V., Petters, M. D., Suda, S. R., Guo, H., Weber, R. J., and Carlton, A. G.: Trends in
538   particle-phase liquid water during the Southern Oxidant and Aerosol Study, Atmos. Chem. Phys.,
539   14, 10911-10930, 10.5194/acp-14-10911-2014, 2014b.
540 Paatero, P.: Least squares formulation of robust non-negative factor analysis, Chemometr. Intell. Lab, 37,
541   23-35, 1997.
542 Paatero, P.: The Multilinear Engine—A Table-Driven, Least Squares Program for Solving Multilinear
543   Problems, Including the n-Way Parallel Factor Analysis Model, J. Computat. Graphic. Statis, 8,
544   854-888, 10.1080/10618600.1999.10474853, 1999.
545 Palm, B. B., Campuzano-Jost, P., Ortega, A. M., Day, D. A., Kaser, L., Jud, W., Karl, T., Hansel, A.,
546   Hunter, J. F., Cross, E. S., Kroll, J. H., Peng, Z., Brune, W. H., and Jimenez, J. L.: In situ
547   secondary organic aerosol formation from ambient pine forest air using an oxidation flow reactor,
548   Atmos. Chem. Phys., 16, 2943-2970, 10.5194/acp-16-2943-2016, 2016.

549   Paulot, F., Crounse, J. D., Kjaergaard, H. G., Kürten, A., St. Clair, J. M., Seinfeld, J. H., and Wennberg,
550   P. O.: Unexpected Epoxide Formation in the Gas-Phase Photooxidation of Isoprene, Science,
551   325, 730-733, 10.1126/science.1172910, 2009.
552   Peng, Z., Day, D. A., Stark, H., Li, R., Lee-Taylor, J., Palm, B. B., Brune, W. H., and Jimenez, J. L.: HOx
553   radical chemistry in oxidation flow reactors with low-pressure mercury lamps systematically
554   examined by modeling, Atmos. Meas. Tech., 8, 4863-4890, 10.5194/amt-8-4863-2015, 2015.
555   Rissler, J., Vestin, A., Swietlicki, E., Fisch, G., Zhou, J., Artaxo, P., and Andreae, M. O.: Size distribution
556   and hygroscopic properties of aerosol particles from dry-season biomass burning in Amazonia,
557   Atmos. Chem. Phys., 6, 471-491, 10.5194/acp-6-471-2006, 2006.
558   Saylor, R. D., Edgerton, E. S., Hartsell, B. E., Baumann, K., and Hansen, D. A.: Continuous gaseous and
559   total ammonia measurements from the southeastern aerosol research and characterization
560   (SEARCH) study, Atmos. Environ., 44, 4994-5004, 2010.
561   Stolzenburg, M., Kreisberg, N., and Hering, S.: Atmospheric Size Distributions Measured by Differential
562   Mobility Optical Particle Size Spectrometry, Aerosol. Sci. Tech., 29, 402-418,
563   10.1080/02786829808965579, 1998.
564   Su, L., Patton, E. G., Vilà-Guerau de Arellano, J., Guenther, A. B., Kaser, L., Yuan, B., Xiong, F.,
565   Shepson, P. B., Zhang, L., Miller, D. O., Brune, W. H., Baumann, K., Edgerton, E., Weinheimer,
566   A., and Mak, J. E.: Understanding isoprene photo-oxidation using observations and modelling
567   over a subtropical forest in the Southeast US, Atmos. Chem. Phys. Discuss., 15, 31621-31663,
568   10.5194/acpd-15-31621-2015, 2015.
569   Ulbrich, I. M., Canagaratna, M. R., Zhang, Q., Worsnop, D. R., and Jimenez, J. L.: Interpretation of
570   organic components from Positive Matrix Factorization of aerosol mass spectrometric data,
571   Atmos. Chem. Phys., 9, 2891-2918, 2009.
572   Wexler, A. S., and Clegg, S. L.: Atmospheric aerosol models for systems including the ions H+, NH4+,
573   Na^+, SO_4^{2-}, NO_3^-, Cl^-, Br^-, and H_2O, J. Geophys. Res., 107, 10.1029/2001jd000451, 2002.
574   Xie, Y., Paulot, F., Carter, W. P. L., Nolte, C. G., Luecken, D. J., Hutzell, W. T., Wennberg, P. O.,
575   Cohen, R. C., and Pinder, R. W.: Understanding the impact of recent advances in isoprene
576   photooxidation on simulations of regional air quality, Atmos. Chem. Phys., 13, 8439-8455,
577   10.5194/acp-13-8439-2013, 2013.
578   Xu, L., Guo, H., Boyd, C. M., Klein, M., Bougiatioti, A., Cerully, K. M., Hite, J. R., Isaacman-VanWertz,
579   G., Kreisberg, N. M., Knote, C., Olson, K., Koss, A., Goldstein, A. H., Hering, S. V., de Gouw,
580   J., Baumann, K., Lee, S.-H., Nenes, A., Weber, R. J., and Ng, N. L.: Effects of anthropogenic
581   emissions on aerosol formation from isoprene and monoterpenes in the southeastern United
582   States, , Proc. Natl. Acad. Sci. USA, 112, 37-42, 10.1073/pnas.1417609112, 2014.
583   You, Y., Renbaum-Wolff, L., and Bertram, A. K.: Liquid–liquid phase separation in particles containing
584   organics mixed with ammonium sulfate, ammonium bisulfate, ammonium nitrate or sodium
585   chloride, Atmos. Chem. Phys., 13, 11723-11734, 10.5194/acp-13-11723-2013, 2013.
586   Zhang, Q., Stanier, C. O., Canagaratna, M. R., Jayne, J. T., Worsnop, D. R., Pandis, S. N., and Jimenez, J.
587   L.: Insights into the chemistry of new particle formation and growth events in Pittsburgh based on
588   aerosol mass spectrometry, Environ. Sci. Technol., 38, 4797-4809, Doi 10.1021/Es035417u,
589   2004.

590

591